Università degli Studi di Napoli "Federico II"

Facoltà di Scienze Matematiche Fisiche e Naturali

Dottorato in Fisica Fondamentale ed Applicata

Measurement of low energy neutrino cross-sections with the PEANUT experiment

Andrea Russo

Relatori:
Prof. Paolo Strolin
Dott. Giovanni De Lellis

Corrdinatore:
Prof. Lorenzo Marrucci

Contents

Introduction

High intensity ν sources for present experiments provide neutrino beams in the few GeV range. This has motivated in the last few years a renewed interest for the study of low energy neutrino cross sections. This study is important also for next generation experiments. They will make use of new types of neutrino beams, designed to provide high intensity sources of few GeV neutrinos. These new sources are the superbeams, which are conventional neutrino beams optimized to maximize their luminosity, the β beams obtained from the β decay of ions accelerated in a decay ring, and the ν factories, where a muon neutrino beam is created using a high intensity muon beam circulating in a decay ring.

Unlike for high energy neutrino cross sections, in the range of energies up to about 5 GeV the available data come mainly from measurements done in the 70s and in the 80s with bubble chambers experiments. Bubble chambers provide a very good reconstruction of final state particles. This makes the systematic uncertainties smaller than other experimental techniques. However, events were reconstructed by hand and bubble chamber neutrino experiments collected poor statistics. Anyway, they offer an important and necessary constraint on model predictions. This situation is now changing with the data of new neutrino experiments. Useful information are coming from both neutrino oscillation experiments like MiniBooNE and K2K, and experiments specifically designed for cross section studies, like $MINER\nu A$.

Moreover, low energy neutrino cross sections provide an insight on the effects of the nuclear structure on the dynamics of the scattering. These effects constitute an additional source of uncertainty in the prediction of ν cross section for heavy nuclear targets. The kinematics of the interaction is affected both by the binding energy of the target nucleons and by the nuclear reinteractions.

The uncertainties in the modelling of ν interactions in the few GeV range are due to the dynamics of this kind of interactions. Its description is complicated since the total neutrino nucleon cross section is given by the sum of three comparable contributions: quasi-elastic (QE), resonance (RES) and deep-inelastic (DIS) neutrino scattering. While ν interactions

are dominated by QE processes at low energies (i.e. $< 1 GeV$) and by DIS processes at high energies, in this intermediate energy range they all show similar contributions.

One way to investigate the neutrino interactions is to measure precisely their topology. In the study of processes involving the production of particles, one of the most important topological variables is the particle multiplicity, which reflects the dynamics of the interaction. For this reason in the past the fetures of the charged-particle multiplicity distributions have been studied in detail in hadronic collisions and in e^+e^- annihilation.

The nuclear emulsion technique combined with automated emulsion scanning, as in the PEANUT experiment described in this thesis, offers a tool to perform a multiplicity measurement in the neutrino sector. The micrometric resolution of emulsion films allow to perform a very good final state particle reconstruction at the single particle level, so their charged multiplicity and pseudorapidities ditribution can be measured with high precision.

The PEANUT experiment was designed to carry out a precise measurement of the topology of neutrino intercaction at low energy using the NuMI neutrino beam, whose spectrum is well suited to perform also cross section studies. The detector is hybrid, being made of nuclear emulsions and scintillating fibre trackers. The hybrid setup combines the high precision tracking performances of nuclear emulsions together with thetime stamp of the electronic detector.

The thesis is organized as follows:

- The few Gev neutrino physics is the topic of the first chapter. Some results from recent neutrino experiments in this sector are shown, and the physical motivation of the PEANUT experiment is described.

- The PEANUT experiment is described in the second Chapter. The features of the NuMI neutrino beam and of the detector are shown. The Emulsion Cloud Chamber technique is explained in detail.

- Nuclear emulsions are the topic of the third chapter. The development of the application of the emulsion technique to particle physics experiment is described. After this introduction, the automated microscopes developed in Japan and in Europe for the scanning of emulsion films are described.

- The procedure for the analysis of neutrino interactions in PEANUT is the topic of the fourth chapter. The scanning procedures for the location of the interaction points of neutrinos inside the emulsion/lead target are discussed. A detailed comparison between the experimental data and a Monte Carlo simulation is shown.

- In the fifth chapter the physics results are described. The measurement of the charged particle multiplicity distribution in neutrino interactions and the evaluation of the various contribution to the total charged current neutrino cross section are presented.

Chapter 1

Low Energy neutrino scattering experiments

1.1 Physics processes

Neutrino-nucleon interactions have been observed over a wide energy range, from a few MeV neutrinos provided by nuclear reactors (or by the sun) up to energies of the order of $\approx 10^2 GeV$, reached with accelerator neutrinos. Deep inelastic neutrino-nucleon processes confirmed the validity of the parton model which emerged from the study of deep inelastic electron-proton scattering, they have been crucial in determining the quantum numbers of the hadron constituents, which led also to the success of QCD as the basic theory of the strong interactions.

The charged current inclusive process is:

$$\nu_l + N \rightarrow l^- + X \tag{1.1}$$

where N is a nucleon, and X is a generic hadronic state.

As for the charged lepton deep inelastic scattering, the main kinematical variables in this processes are the momentum transfer, the Bjorken scaling variable and the inelasticity of the scattering. The differential cross section $d^2\sigma/(dxdy)$ can be expressed in terms of structure function. In this inclusive process, where only the final lepton is observed, the cross section depends on three variables, which are the neutrino energy, the lepton momentum transfer t, and the energy transferred to the hadrons:

$$Q^2 = -t = (p' - p)^2 \tag{1.2}$$

where p and p' are the initial and final hadron momentum, respectively

$$\nu = -\frac{1}{M}qp \tag{1.3}$$

Alternatively, the corresponding Bjorken scaling variables can be used:

$$x = \frac{Q^2}{2M\nu} \tag{1.4}$$

$$y = E' - E \tag{1.5}$$

where E and E' are the initial and final hadron energies, respectively. The amplitude for this process is written as:

$$M_{fi} = -2\sqrt{2}G_W J_l^\mu J_\mu^{hadr} \tag{1.6}$$

where J_μ^{hadr} is the hadronic current and J_l^μ is the leptonic current. The hadronic current contain a vector and axial component:

$$J_\mu^{hadr} = \frac{1}{2}(V_\mu + A_\mu) \tag{1.7}$$

If we consider the quasi elastic (QE) scattering,

$$\nu_l + neutron \rightarrow l^- + proton \tag{1.8}$$

the vector current is:

$$V_\lambda = \overline{u}(p')_P \left[g_V(t)\gamma_\lambda + i\frac{1}{2M}k(t)\sigma_{\lambda\mu}q^\mu + g_S(t)q_\lambda \right] u(p)_N \tag{1.9}$$

where $q = p - p'$, M is the nucleon mass (the mass difference between the proton and the neutron is neglected), and g_V, g_S, k are form factors. In the following, it will be convenient to use the so-called charge and magnetic form-factors:

$$g_E(t) = g_V(t) - \frac{t}{4M^2}k(t) \tag{1.10}$$

$$g_M(t) = g_V(t) + k(t) \tag{1.11}$$

For the axial current, we have two form factors: the axial form factor g_A and the pseudoscalar form factor g_P

$$A_\lambda = \bar{u}(p')_P \left[g_A(t)\gamma_\lambda\gamma_5 + g_P(t)\gamma_5 q_\lambda \right] u(p)_N \qquad (1.12)$$

In the limit of equal masses of the quarks u and d, the isospin symmetry is exact and the vector current is conserved. This is equivalent to the CVC hypothesis of Feynman and Gell-Mann [**?**], which relates the weak current form factors to the electromagnetic current form factors. As a consequence, we have:

$$g_E(t) = (G_E(t))_P - (G_E(t))_N \qquad (1.13)$$

$$g_M(t) = (G_M(t))_P - (G_M(t))_N \qquad (1.14)$$

$$g_S(t) = 0 \qquad (1.15)$$

where $G_M(t)$ and $G_E(t)$ are the electromagnetic form factors.

The axial current is conserved in the limit of vanishing quark masses. Unlike the vector current, the axial one is not related to any other known current, and the axial form factor can be only measured in neutrino scattering experiments.

The cross section for the elastic process is usually written in the Llewellyn Smith formalism as:

$$\frac{d\sigma}{dQ^2} \propto \frac{1}{E^2} \left[A(t) + B(t)\frac{(s-u)}{M_N^2} + C(t)\frac{(s-u)^2}{M_N^4} \right] \qquad (1.16)$$

where A, B and C depend on the vector and axial form factors: s and u are Mandelstam invariants. The axial form factor is usually assumed to have a dipole form:

$$g_A(Q^2) \approx \left[\frac{g_A}{1 + Q^2/m_A^2} \right]^2 \qquad (1.17)$$

The axial mass parameter m_A controls both the absolute and the differential quasi elastic cross sections. This is the reason why a lot of effort is being made in order to reduce the uncertainty on its measurement and to investigate its universality for different nuclear targets.

The resonance production (RES) results in the creation of a single pion via the excitation and subsequent decay of a resonance with mass $1.08 < W(GeV) < 1.4 - 2.0$. Focusing on charged current interactions, the resonances include two possible final states:

$$\nu_l p \to l^- \Delta^{++} \qquad \Delta^{++} \to p\pi^+ \tag{1.18}$$

$$\nu_l n \to l^- \Delta^+ \qquad \Delta^+ \to p\pi^0, \Delta^+ \to n\pi^+ \tag{1.19}$$

Resonance production cross sections are computed using the Rein and Sehgal formalism [2]: the decay matrix elements can be computed or extracted from experimental input. The main source of data are the bubble experiments performed in the 70s and in the 80s, such as BNL [3].

As the neutrino energies becomes larger than about $3 GeV$, the deep inelastic process (DIS)

$$\nu_l + p \to l + X \tag{1.20}$$

becomes predominant. The transition region between resonance production and deep inelastic processes is characterized by the final state hadronic mass in the range $W \approx 1.4 - 2.0 GeV$.

The inelastic cros section for unpolarized nucleons is determined by the spin averaged matrix element squared, and can be expressed as the product of a leptonic tensor times a hadronic tensor W:

$$\sigma \propto L_{\mu\nu} W^{\mu\nu} \tag{1.21}$$

The hadronic tensor is expressed in term of inelastic structure functions:

$$W_{\mu\nu} = \frac{p_\nu p_\mu}{M} W_2(\nu, t) - M g_{\mu\nu} W_1(\nu, t) - \frac{1}{2M} i\epsilon_{\mu\alpha\nu\beta} p^\alpha p^\beta W_3(\nu, t) \tag{1.22}$$

The deep inelastic region is defined by the conditions

$$Q^2 \gg M^2 \quad \nu \gg M, \quad with \quad \frac{Q^2}{\nu} \quad finite \tag{1.23}$$

In this region, scaling is observed (i.e., the structure functions depend only on the adimensional variable $x = \frac{Q^2}{2M\nu}$), and the W functions become:

$$\nu W_2(t, \nu) \to F_2(x) \tag{1.24}$$

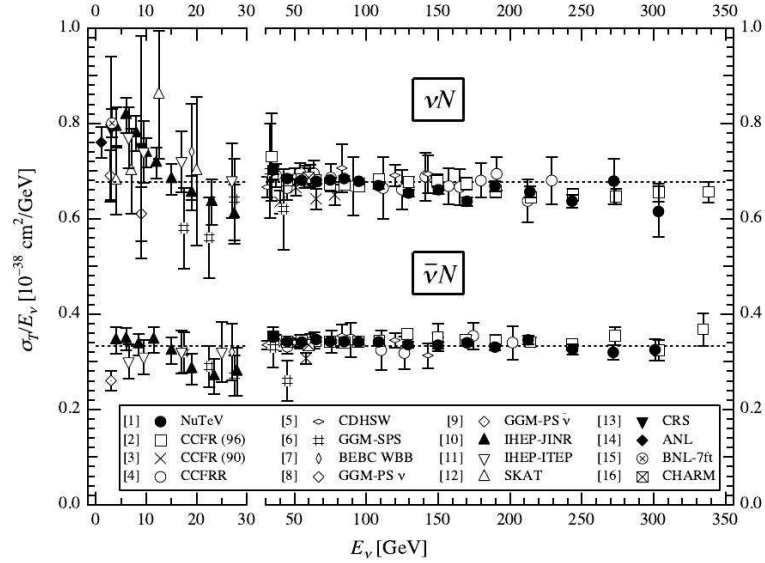$$M W_1(t, \nu) \to F_1(x) \tag{1.25}$$

Figure 1.1: $\frac{\sigma_\nu}{E_\nu}$ for muon neutrino and anti-neutrino as a function of neutrino energy.

$$\nu W_3(t, \nu) \rightarrow F_3(x) \qquad (1.26)$$

with $2xF_1 = F_2$ holding when neutrino interact with spin $\frac{1}{2}$ particles.

A reliable description of the neutrino-nucleon charged current (CC) interaction must take into account all of these three possible dynamics: quesi elastic, resonance production, and deep inelastic scattering. This is easier in the low and in the high energy limit: in the first case the quasi elastic process dominate over the others, while in the second case the deep inelastic process is predominant. The energy interval from $\approx 1 GeV$ to a few GeV is the range where these process have similar cross sections, and the description of the overall neutrino cross section is more complicated. The current state of the measurement of neutrino nucleon cross section from a few GeV to 350 GeV is shown in Fig. 1.1.

1.2 K2K

The K2K experiment [4] did not only verify the evidence for neutrino oscillations previously observed by the Super-K experiment, but it was also the first to publish updated neutrino

cross section measurements in the few GeV energy range using its near detector. It made use of a 1.3 GeV beam produced by the interaction of 12 GeV protons on an aluminum target at KEK.

The K2K near detector consisted of a 1 kton water Cerenkov detector, a scintillating fiber water target tracker (SciFi), a fully active plastic scintillator tracker (SciBar) and a muon range detector (MRD).

Neutrino interactions were studied on two different nuclear targets (carbon and oxygen).

The measurements done by K2K include the measurement of neutral current (NC) π^0 production [5] and the measurement of the axial mass in CC QE interactions in water [6].

Another important result from K2K is a new measurement of the axial mass on carbon from the analysis of QE events collected in the SciBar detector. The result, $m_A = (1.14 \pm 0.11) GeV$ [7], is consistent with the previously published result on water from the K2K SciFi detector, $m_A = (1.20 \pm 0.12) GeV$ [8].

1.3   MiniBooNE

The optimization of the neutrino beam used in the MiniBooNE experiment for the direct search of neutrino oscillations in the LSND region [9] makes the experiment particularly well-suited also for investigations of low energy neutrino interactions. MiniBooNE makes use of both neutrino and antineutrino beams with mean energies of $\approx 800 MeV$, produced by a 8 GeV proton beam.

Using $\approx 2 \times 10^5 \nu_\mu$ QE events, MiniBooNE proved that the widely-used Fermi-Gas model can describe the high statistics MiniBooNE QE data on carbon across the entire kinematic phase space. MiniBooNE is also the first experiment to successfully describe QE data on a nuclear target at low Q^2 . This is accomplished with a two parameter fit, with m_A forcing the agreement between data and prediction at high Q^2 and a parameter k used to adjust the level of Pauli blocking in the Fermi Gas model forcing the agreement at low Q^2 .

MiniBooNE finds that the values of $m_A = (1.23 \pm 0.20) GeV$ and $k = 1.019 \pm 0.011$ provide the best fit to the data [10]. The axial mass value is in agreement with measurements from both the SciFi and Scibar detectors of K2K. The above result for m_A is greater than the value obtained from global fits to past deuterium data, $m_A = (1.014 \pm 0.014) GeV$ [11]. This could have an impact on the estimates of the rate of CCQE events in future ν experiments at low energies.

1.4   MINERνA

Scheduled to start data-taking in 2009, $MINER\nu A$ is a dedicated neutrino cross section experiment planned and approved to run in the 120 GeV NuMI beamline at Fermilab [12]. Making use of the capabilities of the NuMI beam, $MINER\nu A$ will measure neutrino interactions across a wide range of neutrino energies (1-20 GeV). In addition to a fully active fine-grained detector, the experiment will use a variety of nuclear targets (from He to Pb). Using these various targets, $MINER\nu A$ will study nuclear effects in low energy neutrino interactions.

Both K2K and MiniBooNE have revealed systematically higher values of the axial mass from QE data on nuclear targets, assuming a dipole approximation. Anyway, given their neutrino energy spectra, they are only able to study the axial form factor up to Q^2 values of $\approx 2 GeV^2$. $MINER\nu A$, being able to access the high Q^2 region, will be able to investigate deviations of the axial form factors from the dipole approximation. The experiment will probe the axial form factor with a precision comparable to vector form factor measurements performed in electron scattering.

1.5   The PEANUT experiment

The PEANUT experiment was designed with two purposes. The first one is to be a rehearsal of the OPERA experiment, since it exploits the same experimental technique to detect neutrino interactions. The analysis chain of the OPERA experiments includes many steps, from the identification of a neutrino interaction candidate in the detector to the event analysis. PEANUT gave the opportunity to test all the steps of this chain as far as the treatment and the analysis of the emulsion targets is concerned. Infact, the PEANUT detector is made of OPERA-like target modules (called *bricks*), whick were built with emulsions from the same batch as OPERA films. The development chain of these films was also tested at Fermilab, where a facility for the emulsion handling and development, equipped with a dark room, was set up.

Moreover, PEANUT could give a contribution to the study of neutrino interactions occurring in the MINOS [13] detector, which is currently studying atmospheric neutrino oscillations using the NuMI beam. PEANUT is able to reconstruct neutrino events at the single particle level, thus providing important data concerning the charged particle multiplicity and the pseudorapidity distributions of particles created in ν interactions. These data will provide

information useful for the tuning of MC event generator on MINOS.

Furthermore, the emulsion target can be used also to investigate the composition of the NuMI beam and to measure the electron neutrino contamination. The uncertainty on the knowledge of the contamination of ν_e in the NuMI beam is one of the main sources of systematic errors in the measurement of the θ_{13} parameter of the PNMS matrix, which is currently unknown. A second run of PEANUT, with the target modules redesigned in order to maximize the performances in the search for electron neutrino interactions has been also performed, aiming at the electron neutrino contamination measurement in the NuMI beam with a precision of about 10%.

The Emulsion Cloud Chamber technique could also be used in future neutrino oscillation experiments. Infact, they are likely to use few GeV high intensity neutrino beams based on the new technogies which are now under study: the superbeams, the β beams, the ν factories. ECC could serve either as the primary detector or as near detector monitoring the neutrino beam.

Chapter 2

The PEANUT experiment

The PEANUT (Petite-Exposure At NeUTrino beamline) experiment was designed to study low energy neutrino interactions using the NuMi neutrino beam at Fermilab. This beam is well suited to perform this kind of studies, since its energy spectrum covers the few GeV range, where the largest uncertainties in the description of neutrino interaction dynamics arise.

The PEANUT detector is hybrid, since it combines the use of emulsions as high precision trackers and of electronic detectors, namely scintillating fibre planes (SFT). This choice allows to combine the performances of emulsion in the reconstruction of neutrino interactions together with the time stamp information provided by the electronic detector. The target is composed of Emulsion Cloud Chamber (ECC) modules. The ECC consists of a multiple sandwich of passive material (lead) and emulsions, in order to keep the mass of the target sufficiently high to compensate the low neutrino cross-section.

2.1 The NuMI beam

The NuMI neutrino beam at Fermilab is a tertiary beam resulting from the decays of pions and kaons produced in the NuMI target. 120 GeV protons from the Main Injector accelerator are fast-extracted, focused and bent downward by a string of quadrupoles and bending magnets so that they enter the pre-target hall. For construction reasons the pre-target and target halls are located in the dolomite rock formation, requiring the initial trajectory be bent down more than it is actually required to aim at the neutrino beam to the Soudan mine, about 730 km away from Fermilab, where the MINOS detector is located. The neutrino beam is aimed 58 mrad downwars to point towards the MINOS experiment. The size of the proton beam ($\approx 1mm$) is controlled by a set of quadrupoles and are matched to the diameter of the
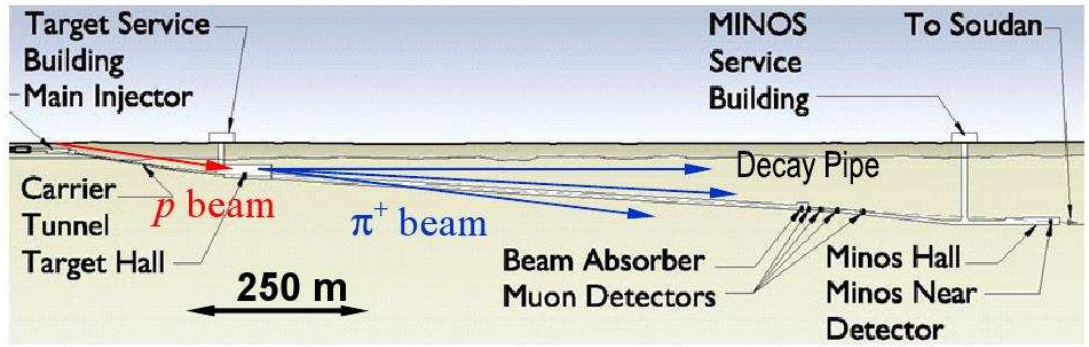
Figure 2.1: Schematic view of the NuMI beamline.

production target.

Protons hitting the target mainly produce mesons that are focused towards the neutrino experimental areas, travel through a long decay pipe and a fraction of them decay to neutrinos and muons. A schematic view of the target hall and of the decay pipe for the decay of secondary mesons is shown in Fig. 2.1. The target is sufficiently long to enable most of the primary protons from the Main Injector to interact, but shaped so that secondary interactions of the pions and kaons are minimized and energy absorption is low. This is achieved with a target that is long and thin, allowing secondary particles to escape through the sides. The focusing is performed by a set of two magnetic horns. The average meson energy is selected by adjusting the locations of the second horn and target with respect to the first horn. This allows to select the energy of the meson beam (and therefore of the neutrino beam) during the course of the experiment.

The particles selected by the focusing horns (mainly pions with a small component of kaons and uninteracting protons) propagate through an evacuated beam pipe (decay tunnel) 1 m in radius and 675 m long, placed in a tunnel pointing downward towards the Soudan mine.

While traversing the beam pipe, a fraction of mesons decay, yielding forward-going neutrinos. A hadron absorber consisting of a water cooled aluminum central core surrounded by steel is placed at the end of the decay pipe to remove the residual protons and mesons. It is followed by a set of beam monitoring detectors. The 240 meters of dolomite rock between the end of the hadron absorber and the MINOS near detector are sufficient to stop all muons coming from the decay pipe.
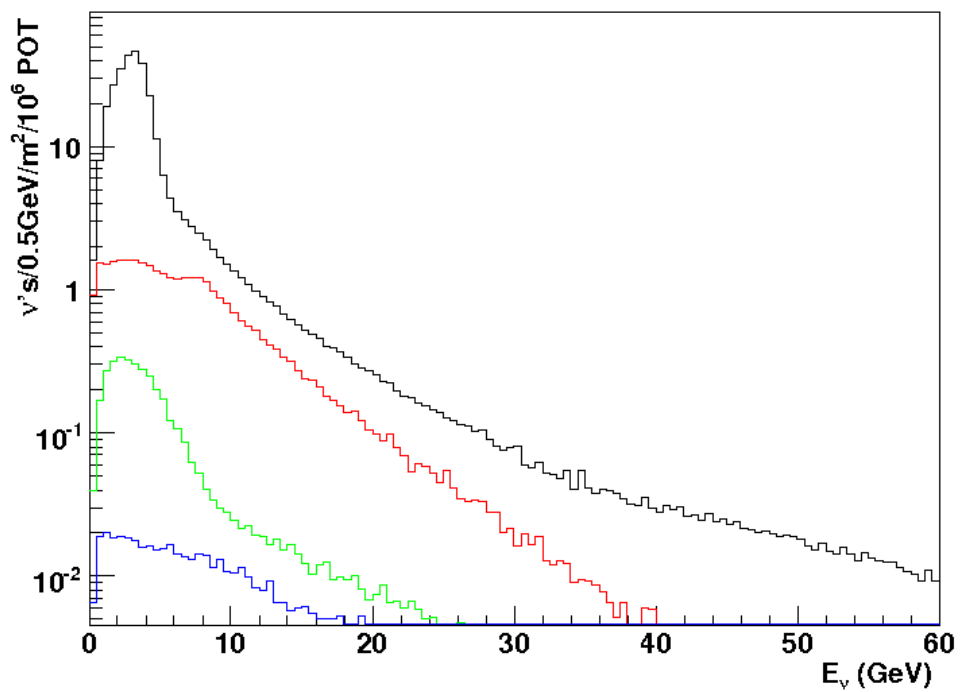
Figure 2.2: Intensity and energy spectrum of the components of NuMI neutrino beam. Black line: ν_μ. Red line: $\overline{\nu}_\mu$. Green line: ν_e. Blue line: $\overline{\nu}_e$
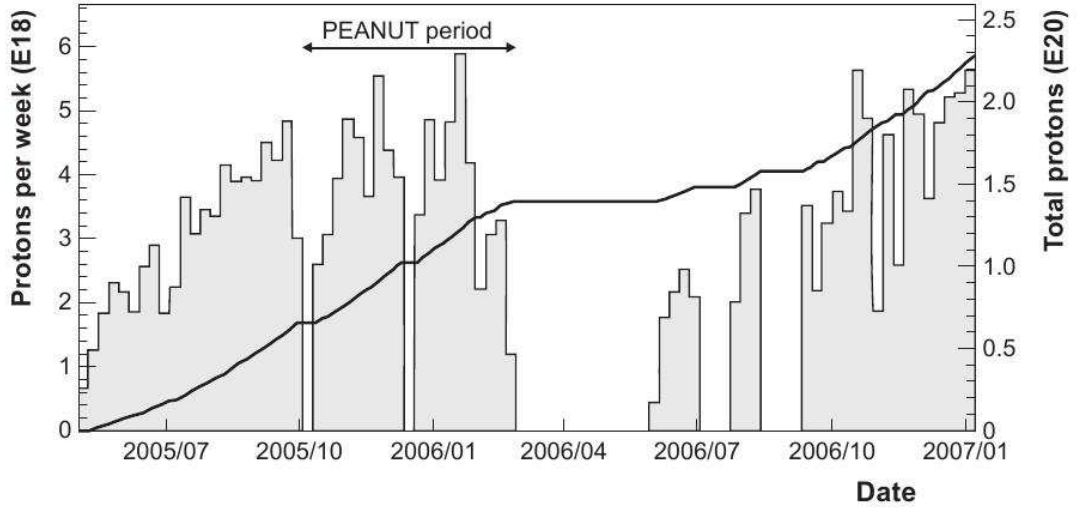
Figure 2.3: Total number of NuMI protons (line) and the protons per week (histogram) delivered on the target during the period from May 2005 till January 2007. The PEANUT exposure is indicated.

The beam is an almost pure ν_μ: contamination comes from smaller components of $\overline{\nu}_\mu$, ν_e, and $\overline{\nu}_e$ coming from pion and kaon decays. Fig. 2.2 shows the energy spectra and the intensity of all the components of the NuMI neutrino beam. Three configuration of target and horn spacings were defined as the low-energy (LE), medium-Energy (ME), and high-energy (HE) beams. The higher-energy beams yield larger number of neutrino interactions as the cross section is higher while the low energy configuration is especially suitable for neutrino oscillation and cross section studies.

Fig. 2.3 shows the total number of NuMI protons (line) and the protons per week (histogram) delivered since May 2005 until January 2007. The rate of events expected is about $1 \nu \quad event/brick/33 \times 10^{17} pots$. The first exposure period of the detector is also emphasized on the plot. During the PEANUT exposure the NuMI beam was in its LE configuration.

2.2   The detector

The emulsion films used in the PEANUT experiment belong to the same batch of films used for the OPERA experiment [15]. They are about $300\mu m$ thick: two emulsion layers of $44\mu m$

are deposited on both sides of a transparent $205\mu m$ thick plastic support. The sensisivity of these films for minimum ionizing particles (i.e. the number of ionized grains per unit path crossed by a particle) is $\approx 30 grains/100\mu m$.

Due to their continuous sensitivity, emulsions start to record latent images due to radiation exposure since their production and until their development. The background coming from these unwanted tracks has been reduced using a procedure called *refreshing* [29], that consists in the treatment of emulsion at high temperature and very high humidity for a few days. The effect of this treatment is to erase on average one third of the grains of previously redorded tracks.

Emulsion films were packed in Emulsion Cloud Chamber modules (ECC), called bricks, similarly to those employed for the OPERA experiment at LNGS [15]. A brick consists of 57 emulsion films: 55 of them are interspaced with 1 mm thick lead plates, while the two most downstream (with respect to the beam) films are placed in contact. These two films are called Special Sheets, and have the role to act as interface trackers between the SFT and the brick. The former, infact, has a resolution of about half a millimiter, while emulsion films have a micrometric tracking resolution. Searching for neutrino interactions in the bricks without the information coming from the analysis of the SS would result into a heavier scanning load.

The transverse dimensions of a brick are $12.5 \times 10.0 cm^2$ (horizontal and vertical direction respectively) while the longitudinal size along the beam axis is $7.5 cm$. The films and the passive material plates are placed orthogonal to the neutrino beam. The lead acts as target for the neutrinos, while the emulsion films serve as tracker for charged particles created in ν interactions. The design of the ECC modules represents a compromise between the two conflicting requirements to build a high density target while keeping the capability to detect short living particles and to reconstruct low energy (i.e., few hundred MeVs) tracks. The design of the structure of bricks is anyway flexible, and different choices in the thickness and the type of passive material are possible. For example, a second run of PEANUT has been performed in the second half of 2007 with the aim to measure the elctron neutrino component of the NuMI beam. In order to maximize the sensitivity of the ECC structure in the search of ν_e events, the structure of the brick has been redesigned: there is an upstream part which uses iron plates as target for the neutrino beam and a downstream part with lead plates acting as a calorimeter region for the electrons produced in ν_e interactions.

The emulsions were sent by plane from their refreshing site in Japan to Fermilab in USA where the ECC were assembled. During their flight from Japan to USA the films integrated cosmic rays. For this reason they were shipped in boxes of 57 sheets in the so-called trans-
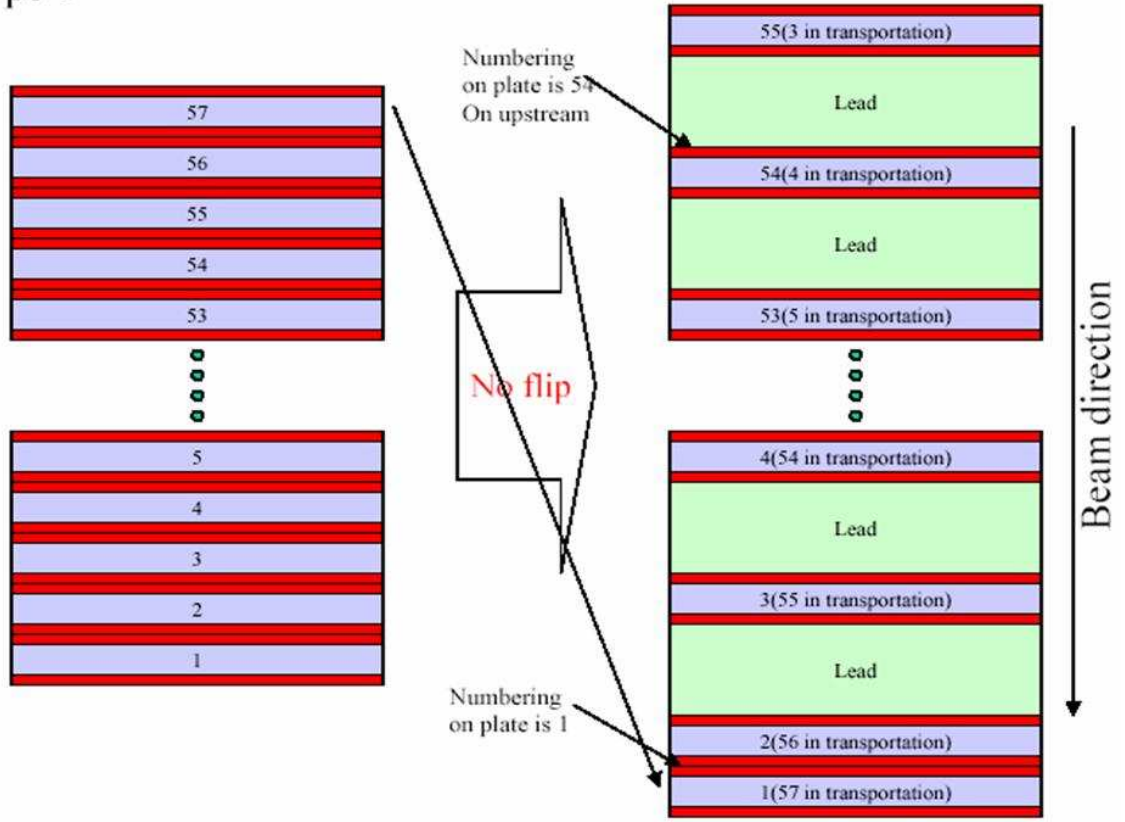
Figure 2.4: Left: film ordering during the transportation (transportation order) Right: film ordering during the beam exposure (assembly order)

portation order. Films from each box were then assembled at Fermilab in the opposite one (assembly order), as shown in Fig. 2.4. The choice to use two different piling orders allows to tag tracks recorded during the transportation, and to ecxlude them from the reconstruction of neutrino events.

The target consists of 4 structures called mini-walls each housing a matrix of 3×4 emulsion/lead target modules, for a total of 48 bricks. The three upstream mini-walls are followed by two planes of Scintillator Fiber Trackers (SFT) each, while the most downstream wall is followed by four SFT planes. Each plane has a transverse area of $0.56m \times 0.56m$, and it is made of horizontal and vertical $500\mu m$ diameter fibres produced by Kururay Co. The SFT are those previously used in the DONUT experiment [14] and provide the transverse coordi-
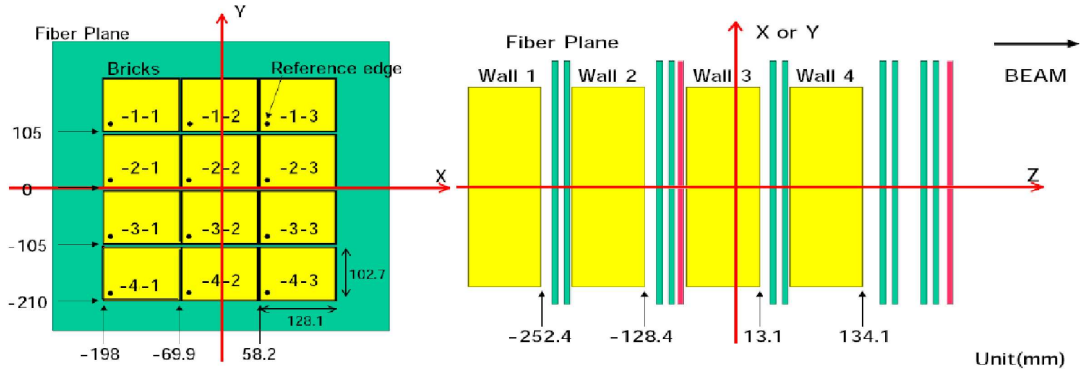
Figure 2.5: Front and side views of the four mini-walls in the PEANUT detector. In the side view, the neutrino beam comes form the left. X-Y SFT planes are shown in green, U planes are shown in violet.

nates of the particle tracks. Moreover, behind the second and fourth mini-walls there are two fibre planes rotated by 45 degrees with respect to the other SFT planes. They are used to disentangle ambiguities in the tridimensional track reconstruction. These fibres are readout by image intensifiers and CCD cameras. Data from the CCD camera are processed at each beam spill by a local PC and stored on disk. The trigger for the acquisition of the SFT data is provided by a signal of the proton kicker extraction magnet of the NuMI beam. The beam spill lasts about $11\mu s$ with a cycle of $1.87s$. A schematical view of the detector is shown in Fig. 2.5.

A total of 160 bricks were produced, most of them with the same geometry adopted for the OPERA bricks. A small fraction of them was produced using iron instead of lead as target in order to make a unbiassed comparison with the data from the MINOS experiment, which also makes use of iron as neutrino target. Since the detector can house only 48 braicks at once, each brick was left in the detector for a period ranging from about two weeks to one hundred days, then removed and substituted with another brick not yet exposed to the neutrino beam. The choice of the exposure time has been done in ordeer to accumulate at least a few tenths of neutrino interactions in each brick.

The data taking period with neutrinos started in September 2005, and ended in March 2006. Each brick was left on the beam for a period ranging from two weeks to about one hundred days. After the exposure, the bricks were brought to the surface laboratory, where they integrated cosmic-rays for a few hours with the aim of collecting a few cosmic rays per

mm^2 for a precise film to film alignment.

The bricks were then unpacked in a dark room, and then brought to an emulsion handling facility. In order to define a local reference frame on each film, a grid of spots was printed on each emulsion before they were developed. Developed films have been shared for the analysis among the various laboratories of the Collaboration.

Chapter 3

The Nuclear Emulsion technique

3.1 Nuclear Emulsions in particle physics experiments

The beginning of the use of photographic emulsions in nuclear and particle physics can be set in 1896, when H.Becquerel placed a slab of phosphorescent substance on a photographic film. He discovered that the phosphorescent substance darkened the emulsion. It meant that the phosphorescent substance emitted a type of ionizing radiation, that we now know to be β rays.

The work carried out by Marietta Blau and Hertha Wambacher to develop the photographic method for particle detection is the most important contribution in the years after Becquerel's discovery. The goals they pursued were the identification of particles, in particular alpha and protons, and the measurement of their energy. The main phisics result was obtained in 1937, with the discovery of "disintegration stars" in emulsion films that had been exposed to cosmic radiation at an altitude of 2300 m above the sea level. These stars were the patterns of spallation events induced by cosmic rays. In 1939, using a batch of half a ton 70 microns thick emulsions exposed to cosmic rays at an altitude of 3500 m above the sea level, Cecil Powell and his collaborators confirmed the results obtained by Blau and Wambacher [16].

The development of nuclear emulsions with higher sensistivity allowed Powell and his collaborators to study particles with higher energies: this led to the discovery of the pion in 1947 [17]. Starting from the sixties, the use of accelerators instead of cosmic ray as source of high energy particles led electronic detectors to gradually replace emulsions.

Nowadays, the development of automated microscopes for the emulsion scanning has brought the emulsion technique to a revival, and they are still used in all the cases where experiments require micrometric tracking precision. Moreover, the scanning speed of the last generation microscopes allows the emulsions to be used to a much larger scale than in the past. The WA17 experiment [18] at CERN and E531 [19] at Fermilab studied the production of charmed particles in neutrino interactions. The same topic was investigated in detail in the CHORUS experiment at CERN [28], designed for the search of $\nu_\mu \to \nu_\tau$ oscillation. The search of beauty particle production induced by pions was perforfed in the WA75 [20] esperiment. τ neutrino interactions have been discovered using this technique in the DONUT experiment [14].The OPERA [15] experiment makes use of a modular emulsion/led target in a 1.2 kton detector for the direct search of $\nu_\mu \to \nu_\tau$ oscillation through the observation of ν_τ appearance in the ν_μ beam from CERN to Gran Sasso.

3.2   The Nuclear Emulsion

Nuclear emulsions are made of crystals of AgBr with a size of the order of $1\mu m$ dispered in an organic gelatine. Silver halide is sensitive to the passage of ionizing radiation: ionized grains can be turned to black silver grains using two chemical treatments, called *development* and *fixing*. These grains have a micrometric size, so they are visible using an optical microscope. A sequence of aligned grains defines a track due to the passage of a charged particle. Nuclear emulsion are in principle similar to photographic films: the basic differences are their larger thickness and a higher sensitivity to ionizing particles. Both these features are required to study the interaction of high energy particles, which have little ionizing power.

The effect of the exposure of nuclear emulsion films to ionizing radiation is the formation of a *latent* image. This image is not stable in time: the higher the temperature and the humidity the lower the lifetime of the image. The cancellation of the latent image (called *fading*) can be exploited in order to delete unwanted tracks recorded in emulsion during storage or transportation: this can be very useful since one of the main feature of emulsion films is their continuous sensitivity, that starts after their production and stops only after the fixing treatment.

The chemical process responsible for the formation of the latent image is the transformation of silver halide crystals into an aggregate of a few silver atoms following the energy deposition due to ionizing radiation. In order to make these aggregates visible, emulsion are developed. The purpose of the development is to reduce all the silver grains forming the

latent image. The choice of the chemical solution and of the treatment duration is done in such a way to maximize the number of developed grains belonging to the latent image while minimizing the development of other crystals, due to thermal excitation (so called *fog* grains). Typical values of the fog grain density are around $5grains/1000\mu^3$.

The second step in the chemical treatment of emulsion is the fixing. It is done with the aim of removing all the residual silver halide crystals. These crystals, if left in the emulsion, would gradually brown it with the effect of worsening the quality of the emulsion.

3.3 Automated Emulsion Scanning

In the very first emulsion experiments, the reconstruction of the interactions occurred in the target was performed by hand. As the emulsion technique developed, the scale of the experiments has grown up to a scale that requires the realization of very fast and efficient automated emulsion scanning systems. Furthermore, in modern experiments emulsions are not used anymore as tridimensional visual detectors. They are used as high precision tracking detectors, so the reconstruction of the interaction af a particle in such a detector requires the analysis of several films, which are exposed orthogonal to the incoming particle beam.

The requirement for the fast analysis of a large amount of emulsion films led to the development of automated microscopes, which are able to perform a tridimensional tomography of emulsions in order to reconstruct the tracks of charged particles that crossed the film. The principle of the automated analysis of emulsion is shown in Fig. 3.1: several images at different depths are grabbed by the microscope, dark clusters are recognized in each image, and tridimensional tracks are reconstructed.

The first prototype of a semi-automated microscope, called DOMS Interface [25], was developed in the 70s. Its working principle was to sample the images taken by the microscope at several different depths regularly spaced. These images were processed in order to recognize the grains in each layer, and then a three dimensional image was reconstructed. The distance between consecutive frames is chosen to be almost equal to the focal depth of the objective, in order to prevent sub or oversamplings.

These basic tracking principles were then applied to the first fully automated system (Track Selector, TS) [26], which was developed at the University of Nagoya in Japan in 1985. Improved versions, called New Track Selector (NTS, 1996) and Ultra Track Selector (UTS, 1998) [27] were later developed. The UTS has been used for the emulsion analysis of the CHORUS [28] and DONUT [14] experiments.
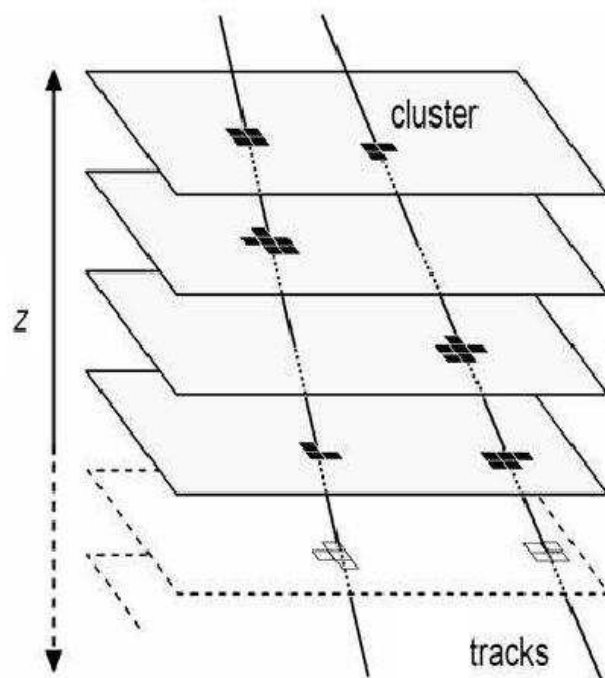
Figure 3.1: Schematic view of the principle of automated emulsion scanning.

The development of a further generation of automated microscopes was driven by the necessisty to cope with the requirement of larger mass scale emulsion experiments, like OPERA. In the OPERA case, the emulsion target is made of $\approx 10^7$ films, for a total area of $\approx 10^5 m^2$. The analysis of such a scale of emulsion films requires very fast emulsion scanning: two different research and development programs have been carried out in Europe and in Japan in order to develop automated microscopes with scanning speed of about $20 cm^2$ and higher.

This led to the development of the European Scanning System (ESS) [22–24] and, in Japan, of the Super Ultra Track Selectror (S-UTS). Both were used for the analysis of the emulsion films of the PEANUT experiment and are now in use for the analysis of the films from the OPERA experiment.

3.3.1 The European Scanning system

The raw data taken by the ESS are the images of the emulsion grabbed at different depths. These images are processed in order to reconstruct clusters of dark pixels due to the silver grains. Information about cluster positions and sizes are stored, and the tracks are then reconstructed by combining grains from different layers with a dedicated software program. The ESS is based on the use of commercial hardware components, using a software-based approach for the emulsion scanning. The software for the data acquisition has been designed to be modular: this approach guarantees the needed flexibility for any future development of the performances of the ESS.

A picture of a ESS microscope is shown in Fig. 3.2. A motor driven scanning table for horizontal movements and a granite arm are fixed to a high mechanical quality table, which provides a vibration-free working surface. The light system is under the table. The way the horizontal stage moves is optimized in order to maximize the scanning speed ($\approx 20 cm^2/h$ for the ESS). This result is achieved by tuning the speed and the acceleration of the stage in order to minimize the sum of the moving time and the vibration settling time. The former is the time needed to move from one field of view to the next one, the latter to wait for oscillations to be dumped below the position resolution. Vertical movements are obtained by a dedicated stage fixed to the granite arm. The optics and the camera for image grabbing are mounted on this stage.
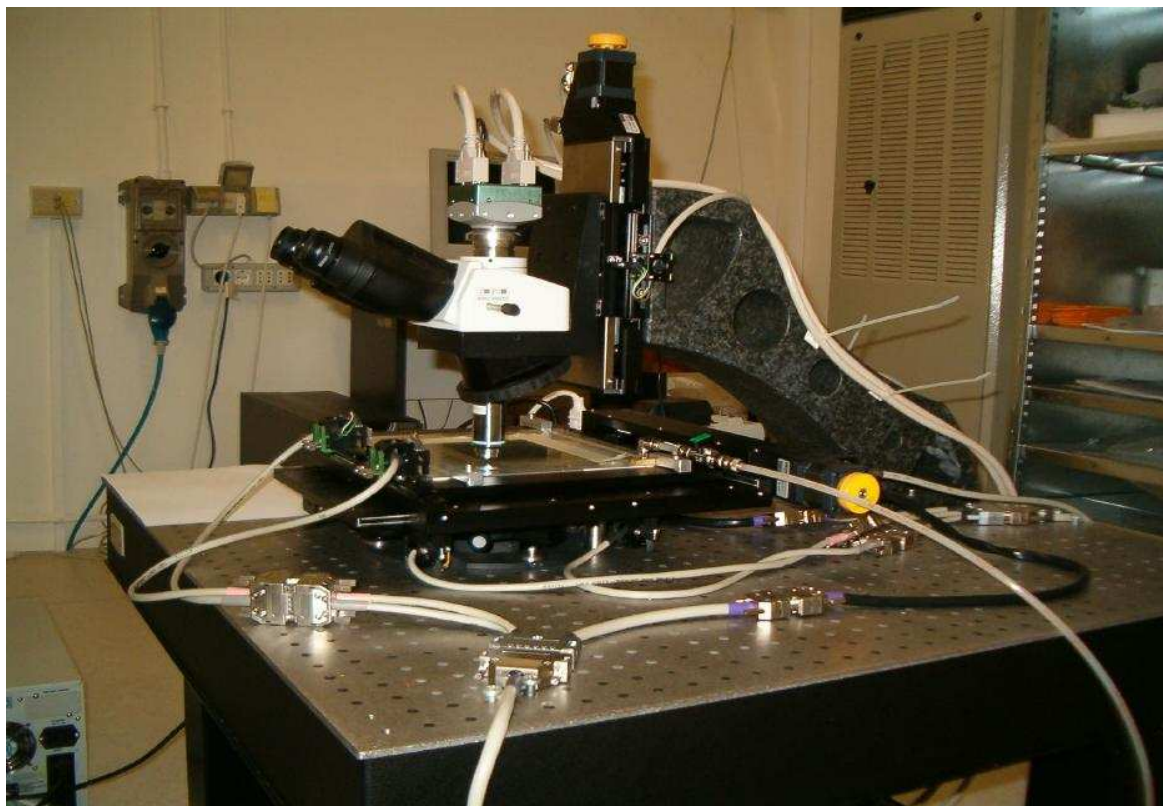
Figure 3.2: A picture of the European Scanning System

Objective

Only few objectives lenses on the market fulfill all the requirements of the ESS: sub-micron resolution and the focusing at different depths. An objective is characterized by the numerical aperture (N.A.), the working distance (W.D.) and the magnification (M). The N.A. defines the resolution that can be achieved by the objective lens: for the ESS, requiring N.A. to be larger than 0.8 turns out in a sub-micron resolution. Moreover, given the $300\mu m$ thickness of the emulsion films used in the OPERA experiment, a $W.D. \geq 0.3mm$ is required. The magnification depends on the size of the image sensor, since one requires a micron to be read by at least a few pixels. In the case of 20 mm wide megapixel sensors used by the ESS, an objective with $M \geq 40$ is needed. On the other side the magnification has not to be much larger than the minimum requirement in order not to reduce the scanning speed.

The last important feature of the ESS objective is to operate in an oil-immersion set-up, so that the light follows an optical path almost omogeneous. This choice has a positive impact on the correction of spherical aberration.

Camera

The scanning speed of $20cm^2/h$ requires a frame acquisition time smaller than 4 ms and a megapixel camera. The ESS is equipped with a Mikrotron MC1310 high-speed megapixel CMOS camera with Full Camera Link interface. Its image sensor is the Micron MT9M413 which delivers up to 10-bit monochrome 1280×1024 images at a speed over 500 frames per second. The sensor size is 20 mm (along the diagonal) and its pixels are $12 \times 12\mu m^2$ large. The features of the camera and of the objective define a field of view of about $390 \times 310\mu m^2$ and image pixels of about $0.3 \times 0.3\mu m^2$: consequently, the image of a focused grain is ≈ 10 pixels large.

The processing board

The frame grabber and the image processor are integrated on the same board, a Matrox Odyssey Xpro. The processor is a Motorola G4 PowerPC supported by a Matrox custom parallel processor. It is equipped with a 1 GB DDR SDRAM memory; the internal I/O bandwidth can achieve over 4 GB per second transfer rate, while the external rate reaches 1 GB per second. A Full Camera Link connection allows an acquisition rate from the camera up to 680 MB/s. At present, a camera frame rate of 377 fps and 8-bit grey level images are used corresponding to an acquisition rate of 471 MB/s. By acquiring 16 frames along the

$44\mu m$ emulsion layer, an acquisition time of about 40 ms is needed for each field of view.

Image processing

A dedicated software to acquire and process the images of nuclear emulsions was developed. It is based on a modular structure where each module has a well defined task (e.g. image grabbing, track pattern recognition and fitting, data I/O handling, etc...). For each field of view the program grabs several images at different depths, recognizes black spots in each image, selects possible track grains, reconstructs tridimensional sequences of aligned grains.

In order to achieve high efficiency in the detection of grains and to keep a good background rejection power, grabbed images are processed in a sequence of steps. First, they are digitised and converted to a grey scale of 256 levels. Then, a procedure based on Point Spread Function (PSF) and on the application of a Finite Impulse Response (FIR) filter [21] is applied in order to enhance dark spots over the background.

The PSF ($\phi(x, y, z)$) function is the 3D distribution of the light intensity due to a point-like obstacle placed at the origin of a reference frame. A real image is the folding of the PSF with the real object distribution. The resulting gray level is obtained by integrating over the volume, the obstacle density N, the flux of light I and the function ϕ. Moreover, in order to enhance the contrast between focused grains and the background, a 2D FIR filter is applied to each image. This is a local operation: each pixel is re-evaluated as a weighted sum of the input values of the neighbourhood pixels, with the weights given by the filter kernel. The Kernel of the filter used is the following matrix:

$$\begin{pmatrix} 2 & 4 & 4 & 4 & 2 \\ 4 & 0 & -8 & 0 & 4 \\ 4 & -8 & -24 & -8 & 4 \\ 4 & 0 & -8 & 0 & 4 \\ 2 & 4 & 4 & 4 & 2 \end{pmatrix} \qquad (3.1)$$

The next step in the processing is the binarisation: pixels with values exceeding a given threshold are classified as black, the remaining ones as white.

An example of the application of the processes described above is shown in Fig. 3.3. At the end of each image processing, binarised images are transferred to the host PC memory. Black pixels are then clustered, and clusters are selected by applying a cut on their area in order to reduce further the background. The centre of each cluster defines the coordinates of the grain reconstructed by the system.
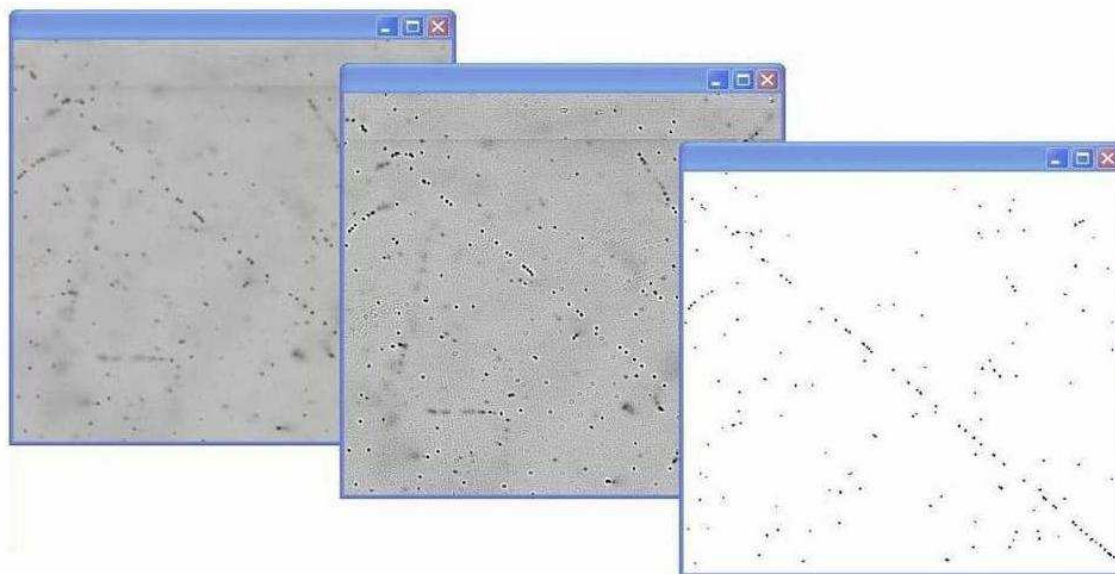
Figure 3.3: Processing of an image grabbed by the ESS. From left to right: grabbed image, filtered image, and selection of black pixels.

Online tracking

The tracking is performed by the PC that drives the ESS microscope and it is optimized in order to maximize the scanning speed. The cycle is divided in two phases: image grabbing and stage displacement to the next field of view. The image clustering starts as soon as the first frame is grabbed and ends a few tens of milliseconds after the end of the grabbing. The remaining time is not enough for tracking: for this reason the tracking is done asynchronously, using the frames grabbed in the previous cycle.

A few thousand of clusters are usually found in each field of view, most of them being background. By applying quality cuts on their size and shape, about 40% of them are rejected. The remaining ones are used as input for the tracking procedure. The tracking consists of two phases: track recognition and track fitting. In the first phase, patterns of aligned clusters are recognized, then a fit of the position of the clusters is performed to evaluate the track slope.

Once all the clusters belonging to tracks are collected, a bidimensional linear fit is performed. Tracks with less than 7 grains are rejected in order to suppress combinatorial background. The number of grains of a track is distributed according to a Poisson distribution

with average value ≈ 13, so this cut discards aboout 2% of the signal.

3.3.2   The S-UTS

One of the main features of the S-UTS is the removal of the stop-and-go process of the stages during the data taking, which is the mechanical bottle-neck for the speed of traditional systems. In order to avoid the stop, the objective lens moves at the constant speed of the stage while moving also along the vertical axis and grabbing images with a very fast CCD camera running at 3000 Hz. The optical system is moved by a piezo-electric device. The camera has a sensor with 512×512 pixels, with a field of view $\approx 120 \times 120 \mu m^2$ to guarantee a resolution of the order of about $0.3 \mu m/pixel$. The very high speed camera provides a data rate of about 1.3 GB/s. This is handled by a front-end image processor which makes the zero-suppression and the pixel packing, reducing the rate to 150300 MB/s. A dedicated processing board makes the track recognition, building tracks and storing them in a temporary storage device with a rate of 210 MB/s. A computer processes the tracks, and writes the output in a database which is used as input for physics analysis. The routine scanning speed is $20 cm^2/h/layer$ while one of the S-UTS systems has reached the speed of $72 cm^2/h/layer$ by using a larger field of view. A picture of the S-UTS system is shown in Fig. 3.4.

3.4   Track reconstruction

The tracking consists of two main phases: track recognition and track fitting. In the first phase, the algorithm recognizes an array of grains as a track, then the track fitting algorithm performs a linear fit of the position of the clusters. The emulsion films used in the PEANUT experiment belong to the same batch of films used for the OPERA experiment. They are about $300 \mu m$ thick: two emulsion layers of $44 \mu m$ are deposited on both sides of a transparent $205 \mu m$ thick plastic support. The automated microscopes performs the tracking separately on the two emulsion layers, and the output of the reconstruction in the two layers is combined only in the offline analysis done after the emulsion scanning.

The basic idea of the tracking algorithm is that a track is an aligned sequence of dark clusters lying at different depths. When two grains are measured in two non-adjacent levels, the pair is used as a track hint: a cylinder with a given radius is considered around the line defined by these two grains, and any cluster within this cylinder is selected. This procedure is shown in Fig. 3.6, and the angular resolution in the reconstruction of microtracks is shown in Fig. 3.7.

Figure 3.4: The Super-Ultra Track Selector.

Since checking each pair of clusters as a track candidate would require a too large computing load, two cuts are applied to select track candidates. The first one concerns the slope of the candidate track, which is required to be smaller than a given value (usually between 0.5 and 1 radian with respect to the direction orthogonal to the emulsion film). The second cut is applied to the minimum number of grains of the candidate track, which is set to 7. Given that the PEANUT emulsion sensitivity for minimum ionizing particles is $\approx 30 grains/100 \mu m$, the number of grains of a track in each of the two 44 μm-thick emulsion layers of PEANUT sheets is distributed according to the Poisson distribution with an average of about 13 grains. The sensitivity is significantly higher for low energy tracks, such as the $\approx 10^2 MeV$ protons accumulated in the films during their flight from Japan to the United States. The effect of the different ionizing power is shown in Fig. 3.5: these are the distributions of the number of grains for tracks recorded in the transportation order, mainly low energy protons accumulated during the flight, and the m.i.p. tracks recorded during the beam exposure are shown. The number of grains of a track is strictly correlated to the particle's ionizing power: for m.i.p. tracks, we expect 25 grains on average (tracks in two consecutive emulsion layers are taken into account in this histogram), for low energy particles the track grains are subsampled because of the high ionizing power, and the distribution is peaked at 32, which is the maximum value measurable by the microscope.

The cut on on the number of grains in the single emulsion layer selects $\approx 2\%$ of the signal. Tracks surviving this cut and the cut on the track slope are then saved in an output file. From this point on, we will refer to them as *microtracks*. After the micro-track selection, multiple reconstructions are rejected: if a grain belongs to two or more micro-tracks, only the track with the highest number of grains is kept.

The following step in the analysis of emulsion data consists of the connection of microtracks in the two layers to form *basetracks*, as shown in Fig. 3.9. This connection reduces strongly the instrumental background, thus significantly improving the signal to noise ratio, and increases the precision of track angle reconstruction by almost one order of magnitude. This linking operation is usually done iteratively: the first trials are used to measure the thickness of the emulsion and to check the data quality.

The basetrack reconstruction is performed by projecting microtrack pairs across the plastic base and searching for an agreement within given slope and position tolerances. The slopes of microtracks are used only to define the angular agreement, since the base-track is defined by joining the microtrack grains which are closest to the plastic base. These points are almost unaffected by distortion effects, and it is the reason why the base-track has an angular
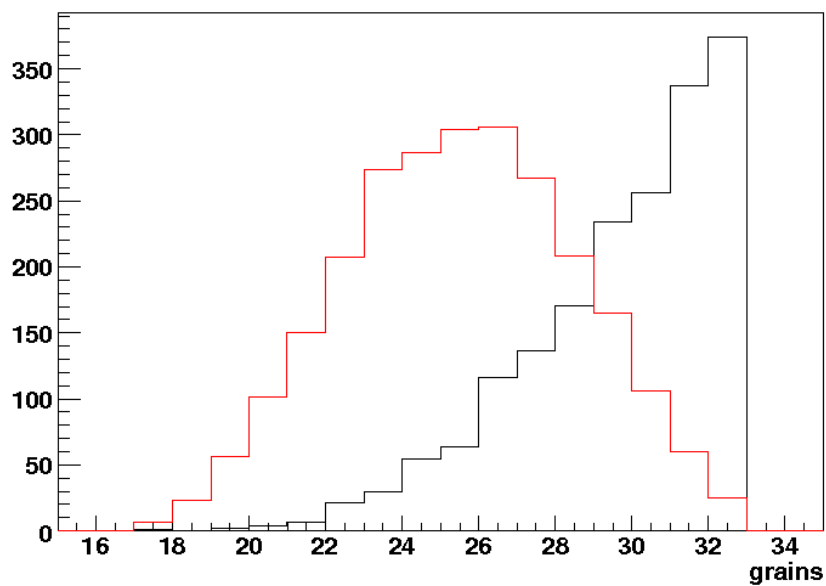
Figure 3.5: Distribution of the grains for basetracks recorded during the flight from Japan to Fermilab (black) and the neutrino beam exposure (red).
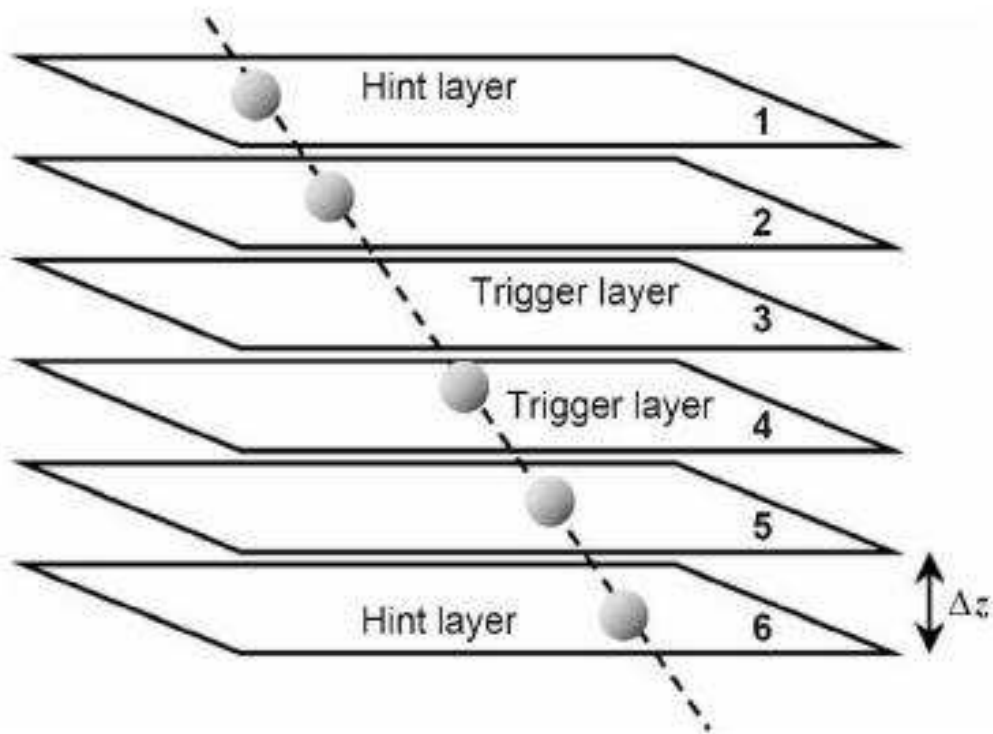
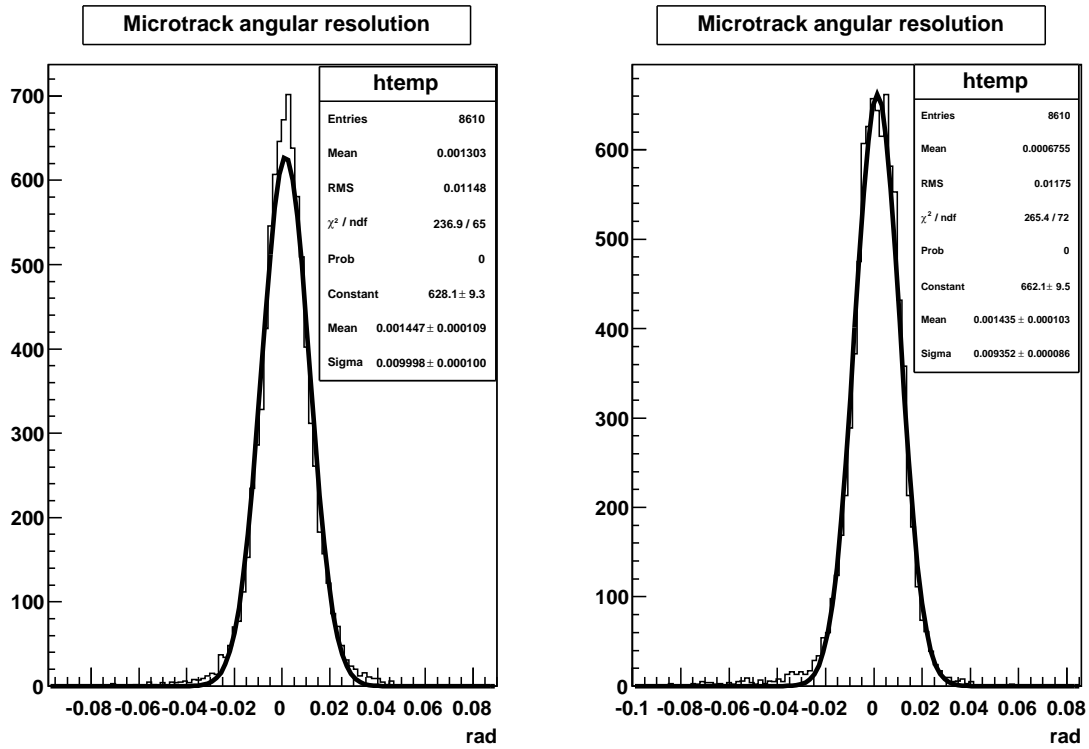Figure 3.6: Schematical drawing of the search for track hints and the tracking procedure.

Figure 3.7: Microtrack angular resolution for vertical tracks in X and Y projections as measured in PEANUT data. The resolution is measured using the slope of basetrack as reference.
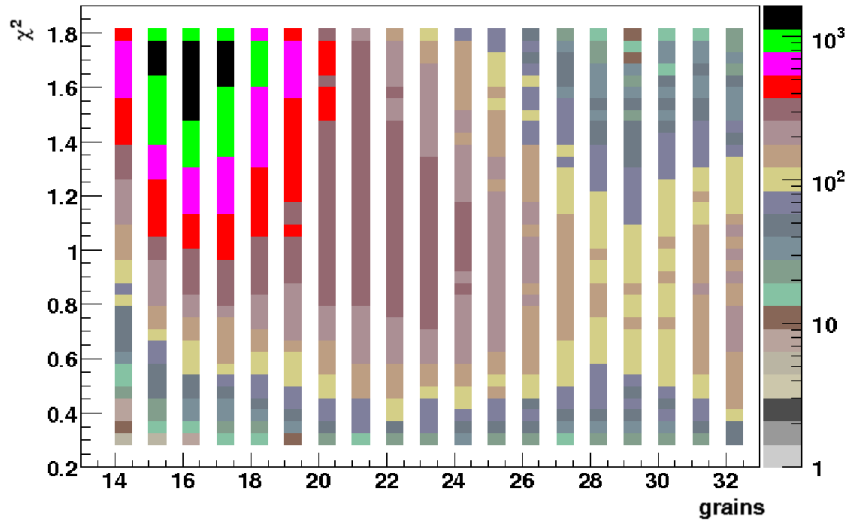
Figure 3.8: χ^2 vs number of grains distribution for basetracks.

resolution much better than microtracks.

The quality of reconstructed basetrack is evaluated with the following χ^2:

$$\chi^2 = \frac{1}{4} \times \left[\frac{(x_1 - x_2)^2}{\sigma_x^2} + \frac{(y_1 - y_2)^2}{\sigma_y^2} + \frac{(\theta_{x1} - \theta_{x2})^2}{\sigma_\theta^2} + \frac{(\theta_{y1} - \theta_{y2})^2}{\sigma_\theta^2} \right] \quad (3.2)$$

where $x_i(\theta)_{x(y)}$ are the position (slope) differences between the two microtracks and $\sigma_{x(\theta)}$ are the position (angular) resolutions.

Fig. 3.8 shows the χ^2 vs the number of grains distribution of basetracks. The separation between the noise (low number of grains, high χ^2) and the signal is clearly visible. Quality cuts in this plane are usually defined in order to reject combinatorial background in the basetrack reconstruction.

The position of tracks in emulsion films is measured with respect to a grid of local reference marks that is printed on each emulsion plate. In order to perform the reconstruction of tracks crossing several films and to exploit the micrometric resolution of emulsion, it is necessary to know the relative position of films during the exposure to the beam, with a precision of few μm. The packing of emulsion in bricks leads to misalignments between consecutive films of the order of several hundreds of μm. For this reason, in the PEANUT standard operation the bricks, after being extracted from the detector, have been exposed to cosmic rays for a
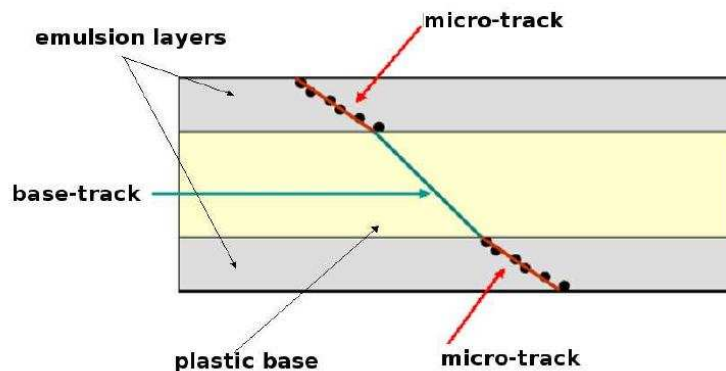
Figure 3.9: A basetrack is obtained connecting two microtracks across the plastic base.

few hours in order to collect enough passing-through tracks to perform a fine plate to plate alignment.

The density of cosmic rays integrated by the emulsion is chosen as a compromise between two conflicting requirements: the need for a precise plate to plate alignment and background density as low as possible. A cosmic ray density of a few tracks per mm^2 can comply with both these requirements. The intercalibration of emulsion films is found by maximizing the number of track coincidences, with the relative displacement parametrized as an affine transformation:

$$\begin{pmatrix} x_{ABS} \\ y_{ABS} \end{pmatrix} = \begin{pmatrix} a_{11} & a_{12} \\ a_{21} & a_{22} \end{pmatrix} \begin{pmatrix} x_{stage} \\ y_{stage} \end{pmatrix} + \begin{pmatrix} b_1 \\ b_2 \end{pmatrix} \qquad (3.3)$$

The use of a large quantity of passing through tracks allows a submicrometric determination of the relative displacements.

Once all emulsion films are aligned, *volume tracks* (i.e., charged tracks which crossed several emulsion films) can be reconstructed. The algorithm for the reconstruction follows various steps. The first one is the search for correlated basetrack in consecutive films. Then, these pairs are tried to be extended on both directions. This track propagation takes into account possible inefficiencies in the basetrack reconstruction: the track finding algorithm allows up to three consecutive missing basetracks before stopping the search.

The algorithm stops when an interaction vertex or a decay is found, or when the track

goes out of the fiducial volume. The track fitting is based on Kalman filtering algorithm.

Chapter 4

Data analysis

4.1   Neutrino event location and reconstruction

The procedure for the reconstruction of neutrino events occurred in the emulsion-lead target has been defined in order to exploit the hybrid features of the detector. The data from the CCD cameras reading the image intensifiers coupled with the SFT are processed at each beam spill, in order to select only ontime events. The trigger for the data processing is provided by a signal of the proton kicker extraction magnet of the NuMI beam, which has a cycle of about 1.87 s. These data are then processed in order to recognize the hits detected by the fibre tracker and to reconstruct charged tracks.

The first step is the reconstruction of charged tracks detected by the tracker fibres, which are built up from the hits recorded by the $500\mu m$ fibres. The reconstruction is performed separately in X and Y projections. The algorithm selects each pair of hits, and defines a cylinder around the line defined by the two hits. If there are more than 6 hits within the acceptance, this track candidate is selected. The track is refitted and all its hits are flagged and discarded for further track formation. This algorithm stops when all candidate tracks are reconstructed in both projections: the result is two samples of bidimensional tracks.

The following phase consists in the merging of bidimensional tracks into tridimensional tracks using the hits recorded in the two U planes. These planes are rotated by 45 degrees with respect to the X and Y planes in order to remove ambiguities. Pairs of bidimensional tracks are merged into a tridimensional track if they have at least one hit in common in any of the two rotated planes.

Only tridimensional tracks were used for the analysis of the events occurred in the bricks. Data from electronic detector are used in order to tag neutrino interactions, by providing a
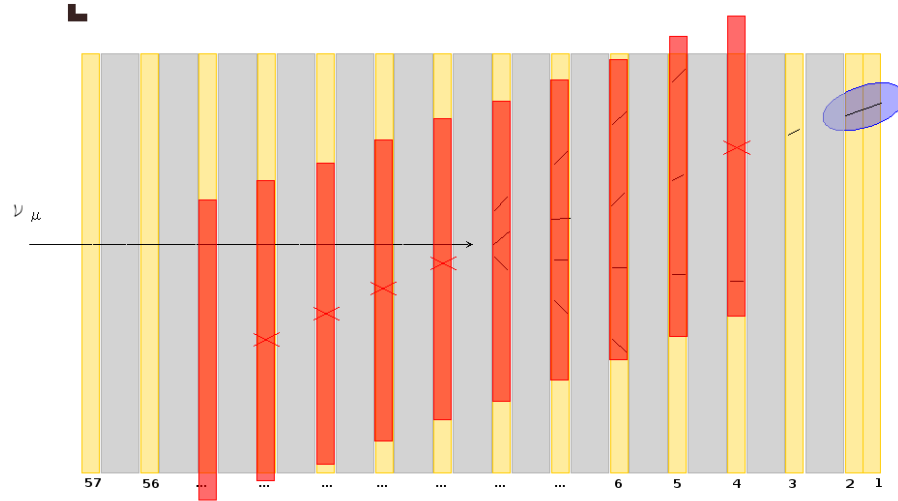
Figure 4.1: Schematical drawing of the scan-back procedure

time stamp for the events stored in the emulsions of the bricks.

The location of neutrino interaction vertices inside the bricks was done following two different approaches: the *scan-back* procedure (used for $\approx 60\%$ of ν events) and a *general scan* method, which are also applied in the OPERA experiment. The first approach requires a matching between tracks reconstructed by the SFT detector and tracks found in the Special Sheets. The matched tracks are then followed up until the vertex is found. The general scan method foresees the scanning of the whole emulsion surface and the reconstruction of all tracks and candidate vertices. The candidate vertices are then validated by the request to have at least one track matched with a tridimensional track reconstructed from the SFT hits.

4.1.1   The scan-back method

The scan-back method is schematically shown in Fig. 4.1. It is based on the scanning of a small area around a predicted point with a narrow angular acceptance. After scanning the whole surface of the two most downstream films, the Special Sheets doublet, all charged tracks within this area are reconstructed by connecting track segments in the two films. The residuals between the track slopes in these films is shown in Fig.4.2. These tracks are originated from particles accumulated during the cosmic ray exposure, muons produces in charged current neutrino interactions occurred in the rock upstream of the detector, and particles from neutrino interactions occurred in the bricks.
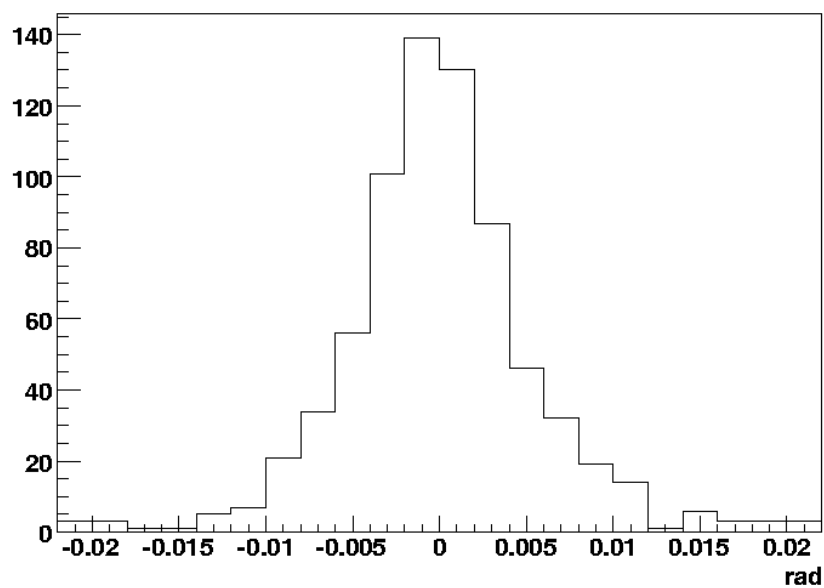
Figure 4.2: Residuals between the track slopes measured in the Special Sheets. The root mean square of the distribution is $\approx 4 mrad$.
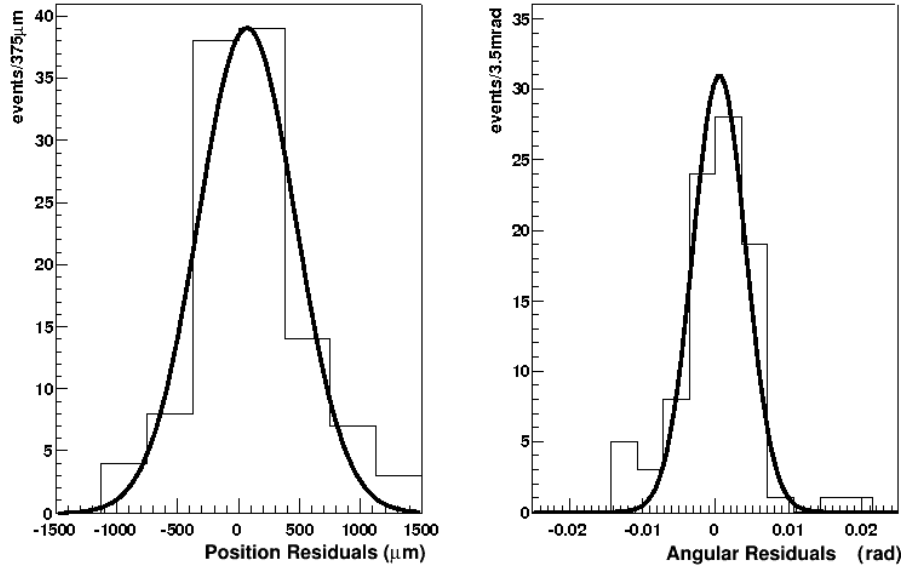
Figure 4.3: Residuals between SFT and emulsion tracks. Left: position residuals ($\sigma = 480\mu m$). Right: angular residuals. ($\sigma = 6mrad$)

The first step of the analysis is to reject all tracks which were not accumulated during the exposure of the brick to the neutrino beam, while keeping particles created in neutrino interactions and rock muons. This goal is achieved by rejecting all tracks without a matching with tridimensional tracks reconstructed in the SFT detector. The matching of emulsion and SFT tracks is defined by a three sigma cut in position and angle with the sigmas shown in the Fig. 4.3

After this cut, the contamination of cosmic muons in the sample of tracks in the SS doublets is reduced by a factor $10^3 \div 10^4$, from $\approx 10^4$ to $\approx 10^1$ tracks. The surviving tracks are used as predictions for the scan-back procedure: they are projected to the upstream emulsion film, and a small area of around $0.01mm^2$ is scanned around each of these points in search for the upstream segment of the track. A precise film to film alignment allows to select these segments within narrow tolerances. These tolerances, as shown in Fig.4.4, are about $8\mu m$ in position and 2 mrad in angle. Once a new segment is found, it is used as a prediction for the track following in the upstream films, and this procedure is repeated until all emulsion films are scanned.

At the end of this procedure we can reject the rock muon tracks: they pass through all
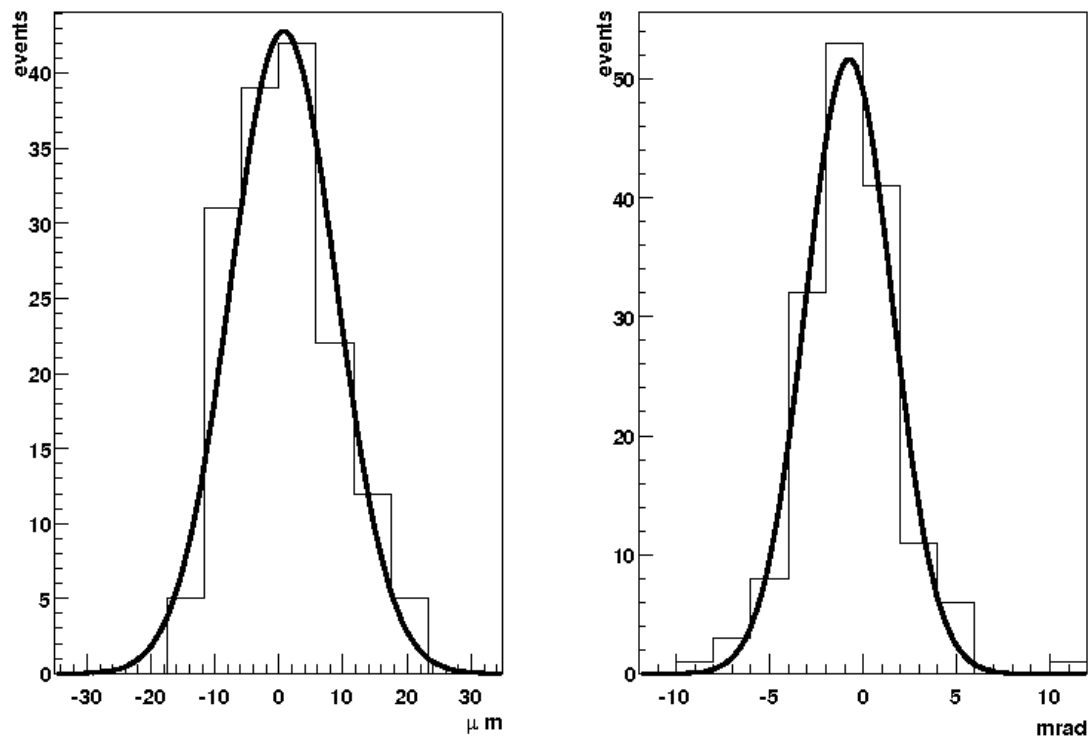
Figure 4.4: Residuals between consecutive segments in scan-back procedure. Left: position residuals ($\sigma = 8\mu m$). Right: angular residuals ($\sigma = 2mrad$).

the emulsion films, while associated to neutrino interactions stop before. In order to account for scanning inefficiencies, a track is defined to stop only after three consecutive films without any basetrack.

The scan-back procedure defines the stopping points produced by neutrino interactions. The following step in the event analysis is the scanning of small volumes around these points. The size of this volume has been optimized using a Monte Carlo simulation in order to allow an efficient reconstruction of all neutrino related tracks with a slope within 400 mrad from the line orthogonal to the emulsion surface. An area of $25mm^2$ is scanned around the coordinates of interaction points for 11 emulsion films, 5 upstream and 5 downstream of the films where the track stops. A volume of $\approx 0.33cm^3$ is analyzed. All the tracks contained in the scanned volume are reconstructed and the vertices are selected on the basis of topological and geometrical cuts. 88 neutrino interaction vertices were located with the scan-back procedure. An example of a neutrino event reconstructed followed this procedure is shown in Fig. 4.5.

4.1.2   The general scan method

The general scan approach consists of performing a large area scan ($\approx 100cm^2$) of each emulsion film of a brick, for a total volume of $\approx 700cm^3$. In each films all candidate basetracks with a slope smaller than 400 mrad are reconstructed. The typical value of the basetrack density at this level is $\approx 30/mm^2$. Most of them are fake basetracks due to combinatorial background, and they are easily rejected by applying quality cuts. The remaining tracks are used in order to perform a fine plate to plate alignment: this operation allows to estimate the relative displacement of consecutive emulfion films during the exposure to the neutrino beam with micrometric precision.

After the alignment, the tracking procedure. This algorithm connects the basetracks belonging to different films and reconstruct the so called volume tracks. This sample of tracks is used as input for the vertexing procedure. Fake vertices due to combinatorial background are rejected by applying cuts on the impact parameter of tracks with respect to candidate vertices. Volume tracks are required to be formed by at least two segments in order to be taken into account in the vertexing algorithm, and only neutral vertices are accepted in the reconstruction, i.e. with no upstream tracks attached to the vertex.

This offline procedure for the reconstrucion of neutrino interactions is performed regardless of the SFT validation, which is applied only a posteriori. Indeed, in order to get the time stamp from the SFT, at least one of the tracks at the vertex has to be penetrating enough to
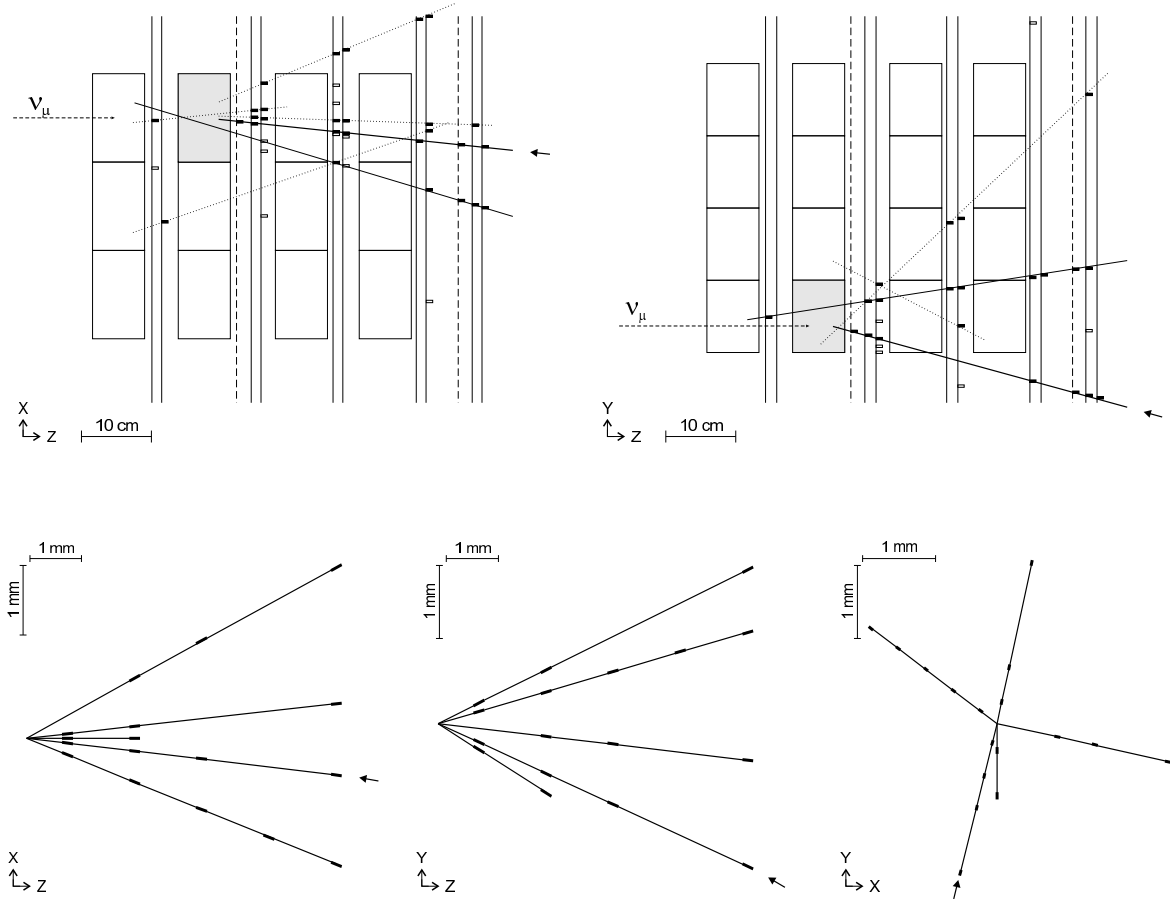
Figure 4.5: Display of a five prong vertex. The reconstruction in the SFT (top figures) and in the emulsions (bottom figures) is shown. For the emulsion reconstruction the front view is also shown. The arrow indicates the emulsion track with a corresponding SFT 3D track. This track is followed back with the scan-back procedure up to the interaction point.
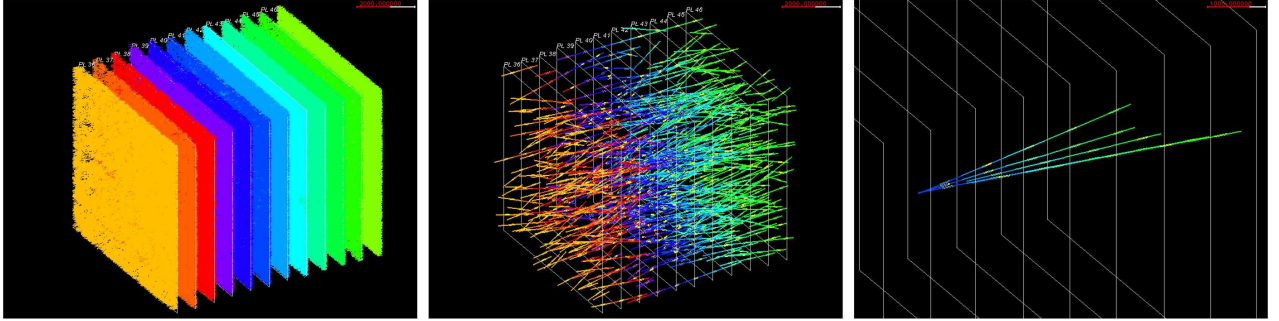
Figure 4.6: General scan approach in the reconstruction of neutrino interactions. From left to right: large area scanning, charged track reconstruction, vertex reconstruction.

reach the downstream end of the brick and to be matched with a SFT track within the same tolerances used in the scan-back procedure.

A total of 59 vertices were located with the general scan method, which is schematically shown in Fig. 4.6. The picture on the left shows the basetracks reconstructed performed in the scanned emulsion films: the density of basetracks after the quality cut is $\approx 10/mm^2$. The picture in the centre shows the volume tracks reconstructed in that fiducial volume. Most of those tracks are cosmic rays or rock muons: the density of volume tracks in PEANUT films is $\approx 4/mm^2$. The last picture shows a candidate vertex found after the application of the vertexing procedure: only tracks originating inside the fiducial volume are used in this procedure.

4.2   MonteCarlo simulation and comparison with data

A Monte Carlo simulation of the detector was developed in the GEANT3 framework [30]. This simulation includes a full description of the geometry of the detector with the four walls and SFT planes. The neutrino event generator [32] has been tuned on the data from the NOMAD experiment.

4.2.1   The event generator

The neutrino event generator for PEANUT, called NEGN, was derived from the event generator developed for the NOMAD experiment, and it is the same as the one used in the OPERA

experiment [15]. The simulation of deep inelastic neutrino interactions is based on a modified version of LEPTO6.1 [36], with the fragmentation parameters retuned on the NOMAD data. This neutrino event generator benefited of the possibility of performing a detailed comparison with the large sample of neutrino interactions detected in the NOMAD detector, which was able to reconstruct the final state of neutrino interactions at the level of single particles. This sample of data allowed to tune the simulation of the hadronic jets, based on the fragmentation parameters and on the inclusion of nuclear rescattering effects.

These effects are also of great relevance in the PEANUT experiment, since the tracking performances of nuclear emulsions allow a precise measurement of the topology of neutrino interactions. Nuclear reinteractions occurring in intra-nuclear cascades of the hadrons produced in the fragmentation process are also simulated, by using the Formation Zone Intra-nuclear Cascade (FZIC) code [37].

The formation zone is related to the time hadrons take to be produced. This effect is introduced in order to account for the suppression of intra-nuclear cascades of high energy hadrons, since the formation time in the laboratory frame is affected by the Lorentz time dilatation and increases by a factor γ. As a consequence, only the low energy hadrons are produced inside the nucleus and are able to interact with the nuclear medium.

Quasi-elastic and resonance production interactions are described by two different sub-generators, respectively based on the Llewellyn-Smith [38] and the Rein-Sehgal models [39]. The simulation of the nuclear reinteraction is taken into account also for these events.

The nucleus is simulated by assigning the coordinates to the nucleons according to the nuclear density profiles and with momenta generated according to the Fermi motion. The nucleon which interact with the incoming neutrino is chosen randomly according to the neutrino-nucleon cross section. The tracking of hadrons is done taking into account possible reinteractions and it is performed until they exit the nuclear region. The modifications of this generator for PEANUT concern the use of a different beam spectrum and of a different target.

4.2.2 The neutrino interactions

The Monte Carlo simulation of the neutrino interactions in the detector includes a full description of its geometry, and it is done in various steps.

The starting point is a *beamfile*, obtained from the event generator NEGN, described in the previous paragraph, according to the NuMI beam spectrum and to the type of target. The information stored in this beamfile include all the identities of the particles produced in

the neutrino interations and their momenta.

Then, the neutrino interaction vertex is placed randomly within the target region defined by the emulsion lead walls. Particles generated at this vertex are then propagated taking into account all physical effects (i.e. including energy loss, secondary interactions, energy losses, etc...). The hits of charged particles crossing the emulsion films and the fibre planes are stored and used as input for the reconstruction softwares.

Microtracks are built up from a fit of the hits in the emulsion layers. In order to perform a reliable simulation of the performances of the reconstruction of the events in the emulsion films, position and slopes of these tracks are smeared according to the resolution measured in real data. Moreover, each microtrack is assigned a number of grains generated according to a Poisson distribution with mean value chosen in order to reproduce the number of grain in emulsion for minimum ionizing tracks.

Microtracks are finally linked into basetracks, and some of them are discarded according to the tracking inefficiency of the scanning system. The dependence of the inefficiency on the slope of the track is also taken into account. This has its minimum for perpendicular tracks and then slowly increases for large angle tracks.

Basetracks obtained using this simulation chain are finally used in the simulation of the reconstruction of neutrino events. The reconstruction software is the same used for real data.

For the SFT detectors the simulation includes the efficiency of the fibres and their resolution, measured using a sample of rock muons crossing the PEANUT detector. The parametrization used in the simulation of the fibres takes into account the dependence of the efficiency on the plane of the fibre tracker and on the position of the track. Also in the case of the SFT, simulated data are reconstructed with the same software used for the data analysis.

4.2.3   MC data comparison

A comparison between data and Monte Carlo events was performed taking into account all the steps of event reconstruction, from the tracking in the electronic detector down to the vertex reconstruction in the ECC bricks.

The ratios of deep inelastic, quasi-elastic and resonance production cross-sections to the total charged current cross section is an important ingredient to build the MC sample used for such a comparison, since some physical quantities are strongly dependent on these values. These ratios are obtained using the following references [33–35], folding these cross sections
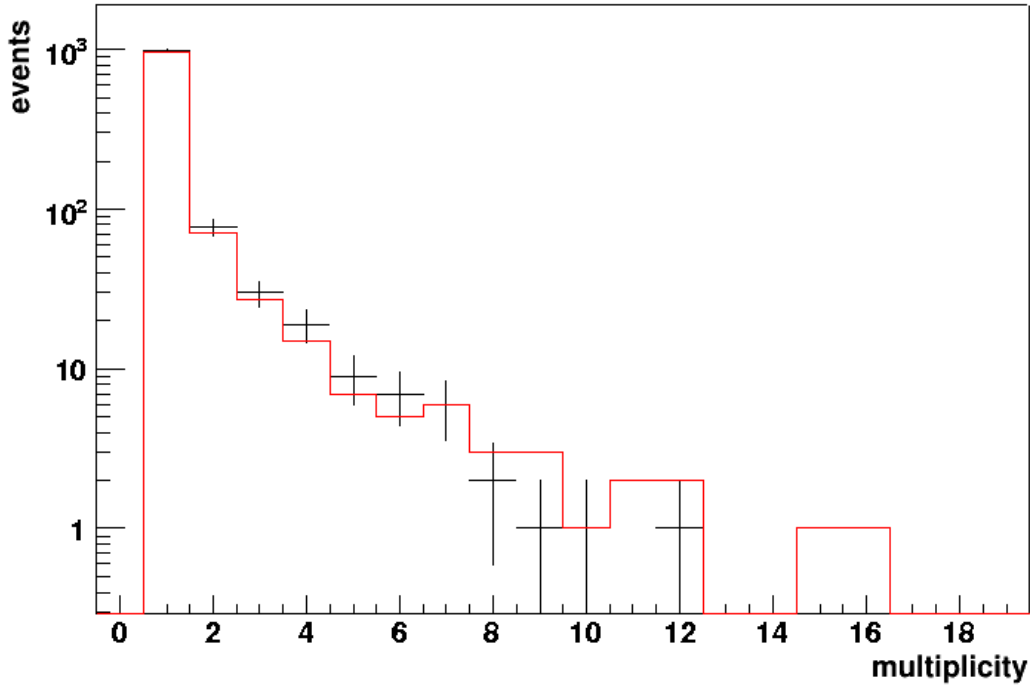
Figure 4.7: Data-MC comparison of the multiplicity distribution of tridimensional tracks reconstructed in the SFT electronic detector (points with error bars are data, the solid histogram shows MC predictions).

measurement with the NuMI beam energy spectrum:

$$\frac{\sigma_{DIS}}{\sigma CC} = 0.70 \pm 0.04 \quad \frac{\sigma_{QE}}{\sigma CC} = 0.19 \pm 0.04 \quad \frac{\sigma_{RES}}{\sigma CC} = 0.11 \pm 0.02 \qquad (4.1)$$

The first step of this comparison concerns the reconstruction of charged tracks related to neutrino events in the SFT detector. The multiplicity distribution of 3D tracks reconstructed by the fibre tracker is shown in Fig. 4.7. Data and MC distributions show a very good agreement through three different orders of magnitude, pointing out that the simulation is based on a reliable description of the detector.

The second step of the neutrino reconstruction is to match the SFT and emulsion tracks: their residuals have been evaluated also on MC, and the results are shown in Fig. 4.8. The distributions are similar to those obtained using data (see Fig. 4.3): in both cases they are well approximated by Gaussians with similar widths.
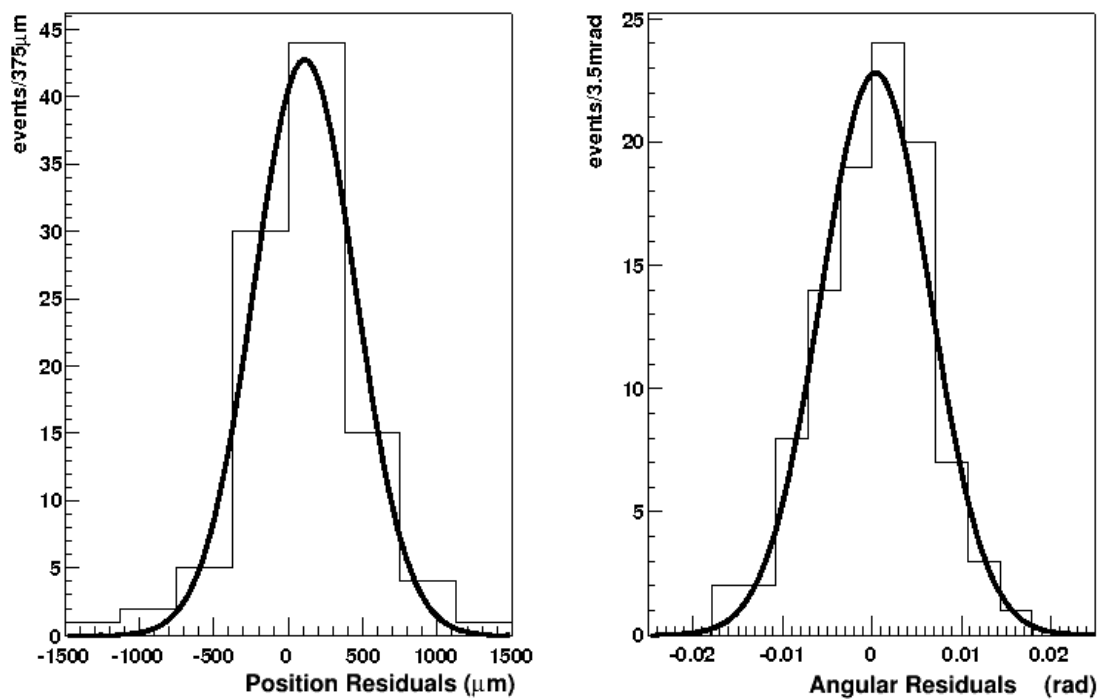
Figure 4.8: Residuals between SFT and emulsion tracks in Monte Carlo. Left: position residuals ($\sigma = 405\mu m$). Right: angular residuals. ($\sigma = 6mrad$)
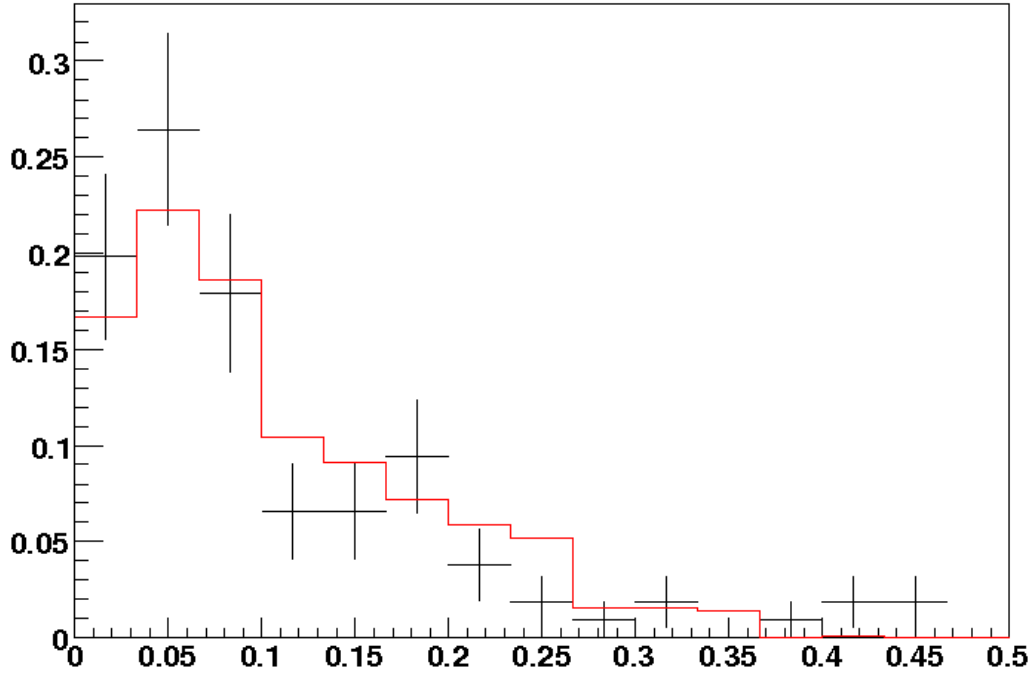
Figure 4.9: Muon slope distribution in neutrino CC interactions in the detector (points with error bars are data while the solid histogram is MC).

In most cases the track followed in the scan-back procedure up to the interaction point is the muon coming from the primary vertex of charged current neutrino interaction. The PEANUT detector has no subsystem dedicated to the muon identification, but the scan-back track is a muon, in about ≈ 0.98 of the cases. The distribution of the slope of the muon in ν_μ CC reconstructed interactions has been compared to the expectations from MC, as shown in Fig. 4.9. The slope of muons is measured with respect to the direction of the neutrino beam, which is not perfectly orthogonal to the emulsion films. The two distributions are compatible within errors.

Chapter 5

Physics results

5.1 Charged particle multiplicity

A total of 147 neutrino interactions were collected in the analysis of PEANUT data. After the location of neutrino interaction vertices inside the lead/emulsion target, a vertexing procedure has been applied in order to reconstruct the topology of these events.

The vertex finding is initiated by the two-track vertices defined according to minimal distance criteria. Topological cuts are used in order to reduce the combinatorial background. The final selection on the track pairs is based on a vertex probability calculated with the full covariance matrix of the involved tracks for the 4 parameters $(x; y; tx; ty)$. Starting from pairs, the n-tracks vertices are constructed using the Kalman Filtering technique. The angular acceptance used in the search prevents the finding of tracks with a slope larger than 400 mrad.

The shape of the reconstructed multiplicity distribution at the primary vertices after the scan-back or general scan procedure is shown in Fig.5.2 together with the MC expectations. MC distribution is obtained assuming the cross sections given in Eq.4.1.

After a detailed MC study, the contribution of neutral current events in the MC simulation has been neglected. The contamination of NC events in the total sample of neutrino events is $\approx 17\%$ at the generator level, then it is reduced to about 4% by requesting at least one 3D track reconstructed in the SFT used to trigger the scan-back procedure or to provide the time stamp for neutrino events reconstructed with the general scan method. This bias is due to the fact that the SFT trackers are more efficient in reconstructing muon tracks than any other hadrons produced in ν interactions. This is explained by two reasons: the first one is that muons have on average higher momenta than hadrons, and the second is that hadrons produced in ν interactions have a not negligible probability to interact in the downstream
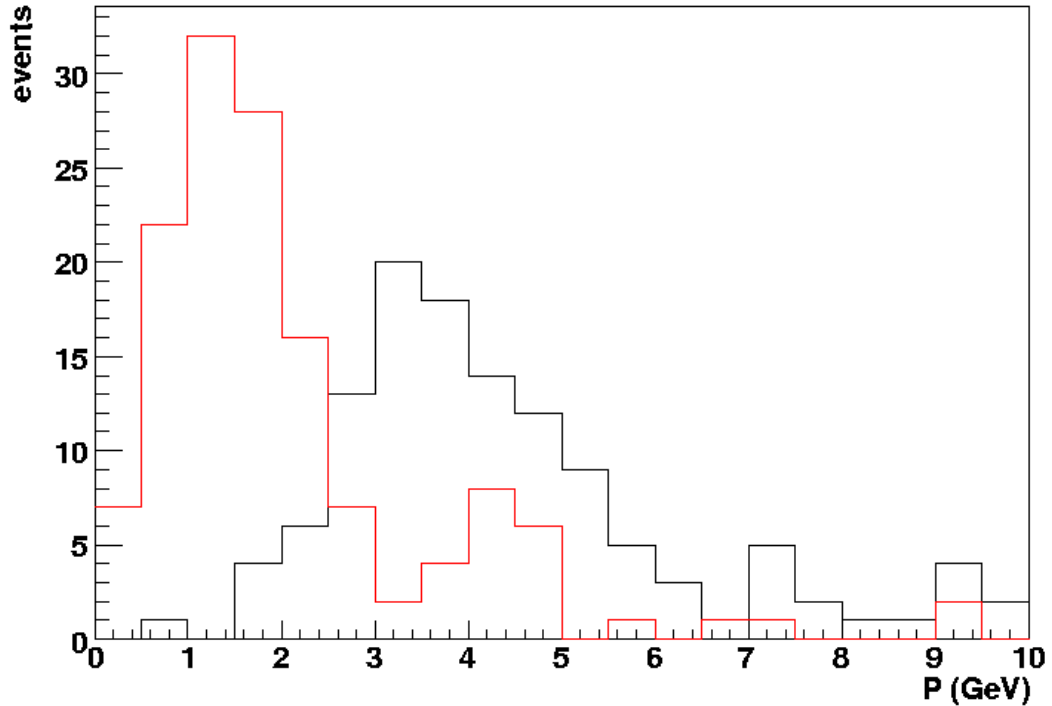
Figure 5.1: Momentum distribution of SFT tracks matched with emulsion tracks. Red: Neutral Current events ($< P >= 2.0 GeV$). Black: Charged Current events ($< P >= 3.8 GeV$).

miniwalls of the detector. An additional bias in favour of charged current events is provided by the matching of SFT tracks with emulsion tracks, so that the neutral current fraction is further reduced to about 1%. This bias is due to the smaller momenta of hadrons in neutral current events which makes the residuals in the matching between emulsions and SFT larger. Fig. 5.1 shows the momentum distribution of SFT tracks matched with emulsion tracks as predicted by the Monte Carlo simulation. Muons show an average momentum a factor of two larger than hadrons.

5.2   Cross sections

We have analyzed the reconstructed events with the aim of disentangling the contributions from deep inelastic, quasi-elastic and resonance production within the total charged current
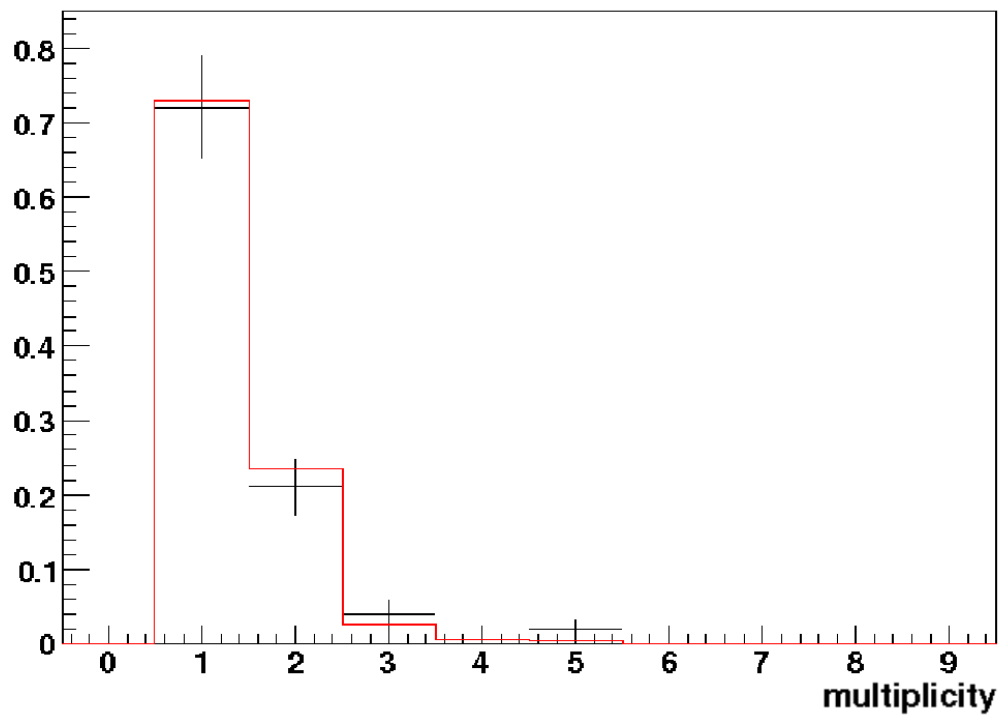
Figure 5.2: The reconstructed charged multiplicity distribution at neutrino primary vertices. Data are the black cross, the red line is the MC expectation. Cross sections in the MC are taken from Eq.4.1.

cross section, exploiting their different shape of the charged multiplicity distribution at the primary ν vertices. The measured charged multiplicity distribution can be then expressed as the sum of the contribution of three distributions. If we consider the ith multiplicity bin, we assume:

$$N_{Data}(i) = A \times (a_{DIS}\epsilon_{DIS}N_{DIS}(i) + a_{RES}\epsilon_{RES}N_{RES}(i) + a_{QE}\epsilon_{QE}N_{QE}(i))$$
$$(5.1)$$

where ϵ_j denotes the reconstruction efficiencies and a_j the fractions of the different scattering processes. $N_{Data}(i)$ and $N_j(i)$ are the ith bin contents of the charged multiplicity distribution in data and MC (separately for DIS, RES and QE events). All these distributions are normalized to one. The factor A is chosen to guarantee that the left and the right term of Eq.5.1 have the same normalization.

The fractions a_i can be estimated by fitting the shape of the MC charged multiplicity distribution to the data. This is obtained by minimizing the following χ^2:

$$\chi^2 = \sum_i \frac{(N_{DATA}(i) - N_j(i, a_j, \epsilon_j))^2}{\sigma_i^2} \qquad (5.2)$$

The MC charged multiplicity distribution depends on 6 parameters: a_j and ϵ_j. The ϵ_j are the reconstruction efficiency evaluated from MC. The fractions are not three free parameters in the fitting procedure, since their sum is fixed to be $\sum a_j = 1$ by their definition. Furthermore, we constraint the ratio of RES to QE events to be $\frac{a_{RES}}{a_{QE}} = 0.58\pm0.16$ [33–35]. This constraint is applied since the study of the charged multiplicity gives little sensitivity in distinguishing QE events from RES events. Given these constraints, the fit depends only on the free parameter a_{DIS} (or, equivalently, $a_{QE} + a_{RES}$). The best-fit values are:

$$a_{QE} = 0.20^{+0.06}_{-0.07}(stat) \pm 0.02(syst) \qquad (5.3)$$

$$a_{DIS} = 0.68^{+0.09}_{-0.11}(stat) \pm 0.02(syst) \qquad (5.4)$$

$$a_{RES} = 0.12 \pm 0.04(stat) \pm 0.02(syst) \qquad (5.5)$$

The a_i values obtained from this fit must be understood as shown in this equation:

$$a_j = \frac{\int \sigma_j(E)\phi(E)dE}{\sum_i \int \sigma_i(E)\phi(E)dE} \quad j = DIS, RES, QE \qquad (5.6)$$

where $\phi(E)$ is the energy spectrum of the NuMI beam.

The uncertainty on the ratio $\frac{a_{RES}}{a_{QE}}$ is the main source of systematic uncertainty in this fit. A number of χ^2 minimizations, with the parameter $\frac{a_{RES}}{a_{QE}}$ varied according to its uncertainty, have been performed in order to estimate this error. It is important to stress that the fit of the multiplicity distribution provides the same value for the deep inelastic fraction even when the constraint on the ratio $\frac{a_{RES}}{a_{QE}}$ is removed.

These results are consistent with the expected values quoted in Eq. 4.1.

5.3 Unfolding of the charged multiplicity and muon slope distributions

The detection efficiency for ν CC events in PEANUT depends on several kinematical and topological variables. The most relevant ones are the energy of the interacting neutrino, the momentum and the slope of the emitted muon, the charged particle multiplicity of the neutrino vertex and the kind of process the neutrino undergoes (QE, DIS, or RES). The reconstruction efficiency affects the reconstructed variables, which do not reproduce anymore the behaviour of the physical distributions. Therefore the data collected in the PEANUT experiment can be used to tune the event generators for neutrino experiments, provided that they are unfolded with the reconstruction efficiency.

Focusing on the charged particle multiplicity distributions, the data distribution can be expressed as:

$$N_{rec}(i) = \left(\sum_j a_j \int \epsilon_j(i, \overline{a}) d\overline{a} \right) N_{true}(i) \qquad (5.7)$$

where $N_{rec(i)}$ is the measured data yield (i is the bin index), $a_{j=DIS,QE,RES}$ are the fractions of the three different processes, and ϵ_j is the reconstruction efficiency which depends on several parameters summarized in the $\overline{a}$ vector. The unfolding operation allows to extract the $N_{true}(i)$ values which best reproduce the observed data distribution taking into account the reconstruction efficiency ϵ.

The efficiences ϵ_j are estimated from the MC simulation. The fractions a_j are taken from Eq.4.1. The uncertainty on the values of a_j is the main source of systematic error in the unfolding. The unfolded charged multiplicity distribution is shown in Fig.5.3 and Table 5.1. Given the limited statistics of high multiplicity events, the bins with multiplicity greater or equal to 5 are grouped together and are not shown in the figure.

Multiplicity bin	fractions
1	(0.35 ± 0.05)
2	(0.21 ± 0.03)
3	(0.16 ± 0.02)
4	(0.033 ± 0.014)
≥ 5	(0.25 ± 0.03)

Table 5.1: Fractions of each bin of the unfolded multiplicity distribution

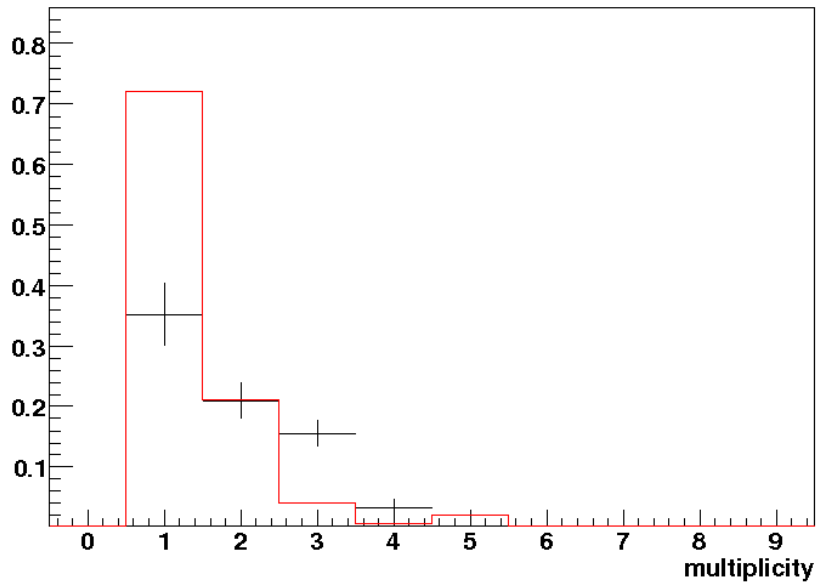Figure 5.3: Charged particle multiplicity distributions normalized to one: before the unfolding (dashed line), after the unfolding (black crosses).

Slope bin	fractions
0-67 mrad	$(23 \pm 3)\%$
67-134 mrad	$(12.6 \pm 1.7)\%$
134-200 mrad	$(16 \pm 2)\%$
200-267 mrad	$(11.9 \pm 1.8)\%$
267-334 mrad	$(8.1 \pm 1.4)\%$
334-400 mrad	$(5.4 \pm 1.0)\%$
≥ 400 mrad	$(23 \pm 4)\%$

Table 5.2: Fractions of each bin of the unfolded muon slope distribution

The same kind of analysis can be extended also to another relevant topological variable, the slope of the muon emitted in a charged current muon neutrino interaction measured with respect to the direction of the neutrino beam. As already mentioned in the previous chapter, the cuts used in the search for ν events select muon tracks with a high purity ($\approx 98\%$), even without a detector specifically designed for the muon identification. The muon reconstruction efficiency in the bricks is affected mainly by the decrease of the emulsion tracking efficiency for large angle tracks.

The results of this unfolding are shown in Fig.5.4, and summarized in Table 5.2. The events with muon slope larger than 400 mrad are grouped together in the table and are not shown in the figure.
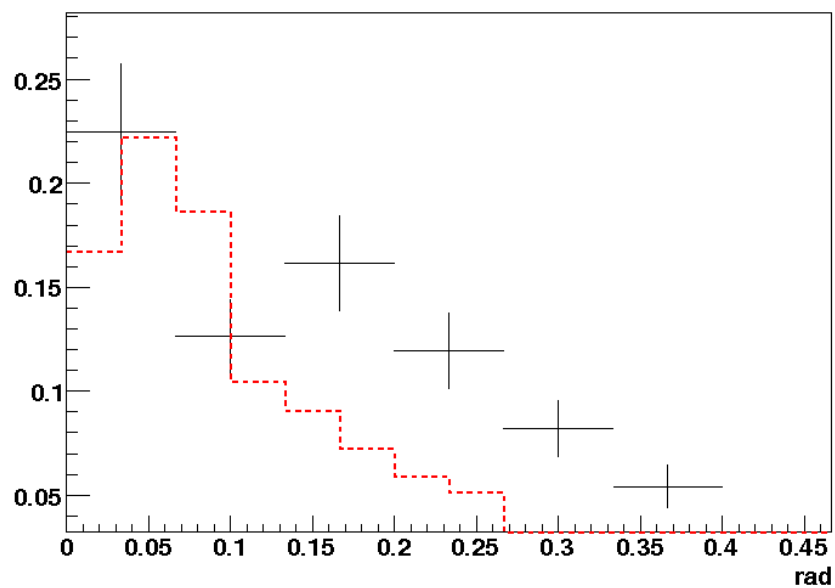
Figure 5.4: Muon slope distributions normalized to one: before the unfolding (dashed line), after the unfolding (black crosses).

Conclusions

The PEANUT experiment was designed to study the ν interactions in the few GeV range using the Emulsion Cloud Chamber (ECC) technique. The ECC technique consists of alternating passive material (lead in PEANUT) plates, which acts as neutrino target, with nuclear emulsion films acting as a high precision tracking device.

The PEANUT detector is hybrid: it combines the use of an emulsion/lead ECC target together with electronic detectors. The ECC detector is divided into modules called *bricks* weighting 8.3 Kg each, for a total mass of about 400 kg. Bricks were placed in four structures called *miniwalls*, each one housing a matrix of 3×4 bricks. The miniwalls were interleaved with scintillating fibre planes, with the task of tracking charged particles created in ν interactions and providing the time stamp information of the events.

The analysis of the nuclear emulsions employed in PEANUT has been carried out using last generation automated microscope systems, having a scanning speed one order of magnitude larger than in the past: the European Scanning System (ESS) and the Japanese S-UTS.

The main physics goal of PEANUT was to measure the contribution of Deep Inelatic (DIS), Quasi Elastic (QE) and Resonance production (RES) processes to the total charged current neutrino cross section. This measurement is important for future neutrino oscillation experiments, which will use high intensity neutrino sources in the few GeV energy range. A better knowledge of neutrino cross section at this energy is needed in order to optimize the performances of next generation neutrino experiments.

The emulsion technique gives the possibility to reconstruct the topology of ν events with high accuracy and small systematic uncertainties. Therefore, the cross section measurement in PEANUT was based on the study of the particle multiplicity in ν interactions. The shape of the measured charged particle multiplicity distribution is particularly sensitive to the contribution of DIS neutrino scattering to the total neutrino cross section. In this process, the multiplicity of charged hadrons produced in the interactions can be large, depending on the mass of the final hadronic state, while in QE and RES the multiplicity is not larger than

two, in the case of excitation and decay of a Δ^{++} state.

In this thesis we have reported on the first data sample collected by the experiment. The last generation automated microscopes for the emulsion scanning were employed for the analysis of emulsion films. The data sample yielded a total of 147 neutrino events. The analysis procedure for the location and the study of the neutrino interaction vertices was applied to the emulsion/lead targets of the detector.

The topology of these events was studied with the aim to measure the distributions of the multiplicity of charged hadrons produced in charged current neutrino interactions and the pseudorapidity distribution of the emitted muons. The performances of the detector were evaluated using using a Monte Carlo simulation of the detector. The DIS fractional contribution to the total charged current neutrino cross section is evaluated to:

$$a_{DIS} = 0.68^{+0.09}_{-0.11}(stat) \pm 0.02(syst) \tag{5.8}$$

This value is compatible with the data obtained in previous experiments using different experimental techniques. The largest contribution to the uncertainty on this measurement comes from to the limited statistics of the data sample collected by the experiment. The use of the ECC technique in a larger scale PEANUT-like experiment could reduce the overall uncertainty by a factor of at least two.

We have also performed the unfolding of the charged multiplicity and muon pseudorapidity distributions in charged current ν events with the neutrino event detection efficiency. The good particle reconstruction with the ECC technique makes the systematic uncertainties smaller than with other experimental techniques. Therefore, although with a limited statistics, these data can be used to tune event generators used in present experiments on the NuMI neutrino beamline at Fermilab and on future neutrino experiments.

Bibliography

[1] B.T. Cleveland et al., Update on the measurement of the solar neutrino flux with the Homestake chlorine detector, Nucl. Phys. Proc. Suppl., Vol. 38 (1995), 47-53

[?] R. P. Feynman and M. Gell-Mann, Phys. Rev. 109:193,1958

[2] Dieter Rein, Lalit M. Sehgal, Neutrino Excitation of Baryon Resonances and Single Pion Production, Annals Phys.133:79,1981.

[3] P. Berge et al., Z Phys. C35, 443(1987)

[4] K2K collaboration, "K2K (KEK to Kamioka) neutrino - oscillation experiment at KEK PS", KEK-PREPRINT-97-266, Jan 1998. 8pp. e-Print: hep-ex/9803014

[5] Nakayama Y et al. (2005) Phys. Lett. B 619 255

[6] Gran R et al. (2006) Phys. Rev. D 74 052002

[7] Espinal X and Sanchez F (2007) AIP Conf. Proc. 967 117

[8] Gran R et al. (2006) Phys. Rev. D 74 052002

[9] C. Athanassopoulos et al, Phys.Rev.Lett. 77:3082-3085 (1996)

[10] Aguilar-Arevalo A et al. (2007) Phys. Rev. Lett. 100 032301

[11] Bodek A et al. (2008) J. Phys. Conf. Ser. 110 082004

[12] Drakoulakos D et al. Preprint hep-ex/0405002

[13] MINOS Collaboration, Phys.Rev.Lett.97:191801,2006.

[14] K. Kodama et al., Phys. Lett. B 504 (2001) 218-224

[15] R. Acquafredda et al., OPERA Collaboration, JINST 4 (2009) P04018

[16] W. Heitler, C.F. Powell, H. Heitler, Nature 146:65-65,1940

[17] C.M.G. Lattes, G.P.S. Occhialini, C.F. Powell, Nature 160:453-456,1947.

[18] D. Allasia et al., Nucl Phys. B 176 (1980) 13.

[19] N. Ushida et al., Nucl. Instr. Meth. 224 (1984) 50.

[20] S. Aoki et al., Nucl Instr. Meth. A 274 (1989) 64.

[21] N. Armenise et al., Nucl. Instrum. Meth. A 551, 261 (2005)

[22] G. Rosa et al., Nucl. Instrum. Meth. A394 (1997) 357.

[23] N. Armenise et al., Nucl. Instrum. Meth. A551 (2005) 261.

[24] M. De Serio et al., Nucl. Instrum. Meth. A554 (2005) 247.

[25] Aoki Shigeki, Niwa, Kimio, Uchusen Kenkyu 27:4 (1984)

[26] S. Aoki et al., Nucl. Instr. Meth. B 51 (1990) 466. (in Japanese)

[27] T. Nakano, Ph. D. Thesis, University of Nagoya, 1997.

[28] E. Eskut et al. (CHORUS Coll.), Nucl. Instr. and Meth. A401 (1997) 7.

[29] T. Nakamura et al., Nucl. Instrum. Meth. A556 (2006) 80.

[30] R. Brun, R. Hagelberg, M. Hansroul, J. C. Lassalle, Geant: Simulation Program For Particle Physics Experiments. User Guide And Reference Manual, CERN-DD-78-2-REV, CERN-DD-78-2, Jul 1978. http://wwwasd.web.cern.ch/wwwasd/geant/

[31] Sacha E. Kopp, The NuMI neutrino beam at Fermilab, AIP Conf. Proc. 773 (2005) 276-278.

[32] D. Autiero, Nucl. Phys. Proc. Suppl. 139 (2005) 253.

[33] S. J. Barish et al., Phys. Lett. B66 (1977) 291.

[34] N. J. Baker et al., Phys. Rev. D23 (1981) 2499.

[35] W. Lerche et al., Phys. Lett. B78 (1978) 510.

[36] G. Ingelman et al., DESY 96-057 (1996).

[37] J. Ranft, DPMJET version II.3 and II.4, INFN/AE-97/45, (1997).

[38] C.H. Llewellyn Smith, Phys. Rep. 3 No. 5 (1972) 261

[39] Dieter Rein, Lalit M. Sehgal, Neutrino Excitation of Baryon Resonances and Single Pion Production, PITHA 80/10, (1980) Published in Annals Phys.133:79,1981.